

## 4 | Why are we still using 3D masses for cluster cosmology?

Based on

Stijn N. B. Debackere, Joop Schaye, Henk Hoekstra, Katrin Heitmann,  
Salman Habib

*Monthly Notices of the Royal Astronomical Society, Volume XXX, Issue Y,  
pp.ZZZ*

The abundance of clusters of galaxies is highly sensitive to the late-time evolution of the matter distribution, since clusters form at the highest density peaks. However, the 3D cluster mass cannot be inferred without deprojecting the observations, introducing model-dependent biases and uncertainties due to the mismatch between the assumed and the true cluster density profile and the neglected matter along the sightline. Since projected aperture masses *can* be measured directly in simulations and observationally through weak lensing, we argue that they are better suited for cluster cosmology. Using the Mira–Titan suite of gravity-only simulations, we show that aperture masses correlate strongly with 3D halo masses, albeit with large intrinsic scatter due to the varying matter distribution along the sightline. Nonetheless, aperture masses can be measured  $\approx 2 - 3$  times more precisely from observations, since they do not require assumptions about the density profile and are only affected by the shape noise in the weak lensing measurements. We emulate the cosmology dependence of the aperture mass function directly with a Gaussian process. Comparing the cosmology sensitivity of the aperture mass function and the 3D halo mass function for a fixed survey solid angle and redshift interval, we find the aperture mass sensitivity is higher for  $\Omega_m$  and  $w_a$ , similar for  $\sigma_8$ ,  $n_s$ , and  $w_0$ , and slightly lower for  $h$ . With a carefully calibrated aperture mass function emulator, cluster cosmology analyses can use cluster aperture masses directly, reducing the sensitivity to model-dependent mass calibration biases and uncertainties.

## 4.1 Introduction

The next decade of cosmological galaxy surveys such as *Euclid*<sup>1</sup> and the Rubin Observatory Legacy Survey of Space and Time (LSST)<sup>2</sup> will elucidate the late-time evolution of the Universe by measuring the large-scale distribution of galaxies out to a redshift of  $z \approx 2$ . The sheer volume of these surveys will result in the detection of over a billion galaxies that can be used to trace the underlying dark matter distribution. The main focus of these surveys is on measuring the matter distribution through the clustering of galaxies and through the lensing-induced distortion of galaxy shapes due to the intervening large-scale structure, the cosmic shear.

Galaxy clusters, located at the most significant peaks of the density field, will be another particularly powerful probe. Due to the hierarchical growth of structure, the abundance of clusters as a function of mass and time depends sensitively on the amount of matter,  $\Omega_m$ , how clustered it is,  $\sigma_8$ , and also on the late-time expansion due to dark energy, quantified by its equation-of-state parameter  $w_0$  and its time derivative  $w_a$  (e.g. Haiman et al., 2001; Allen et al., 2011; Pratt et al., 2019). More than  $10^5$  galaxy clusters will be detected in the coming decade (e.g. Sartoris et al., 2016), transforming galaxy cluster cosmology into a cosmological probe limited only by our understanding of its systematic uncertainties (e.g. Köhlinger et al., 2015).

4

Observationally, clusters are identified as highly significant peaks in maps of some observed signal,  $\mathcal{O}$ , that traces the total mass distribution, such as the galaxy overdensity, the weak lensing shear, the X-ray emission, or the Sunyaev-Zel'dovich (SZ) effect signal. Next, after some quality cuts on the cluster candidates, we are left with a cluster catalogue for the surveyed volume. To derive cosmological constraints from this catalogue, we need a theoretical prediction for the cosmology-dependent cluster abundance, and a way to link the theoretical predictions to the observed clusters. In principle, any halo property that depends on cosmology can be used, but the halo mass,  $\mathcal{M}$ , is the most obvious candidate. This then requires knowledge of the dependence of the halo mass function,  $n(\mathcal{M}|\boldsymbol{\Omega})$ , on the cosmological parameters,  $\boldsymbol{\Omega}$ , the mass–observable relation,  $P(\mathcal{O}|\mathcal{M})$ , and the cluster selection function,  $\mathcal{S}$ . Any systematic error in these quantities will degrade the cosmological constraints from cluster cosmology.

To calibrate the mass–observable relation, we need observational measurements of the halo mass,  $\mathcal{M}$ , for a subsample of the detected clusters. We will denote the halo mass inferred from observations as  $\mathcal{M}_{\text{obs}}$ . There are multiple ways in which halo masses can be defined, since haloes do not have clear boundaries. Weak lensing observations have become the de facto standard to calibrate cluster masses as they provide the only way to directly probe both baryonic and dark matter (for a review, see Hoekstra et al., 2013). Masses can be obtained from weak lensing observations either by fitting a density profile to the observed shear and

---

<sup>1</sup><https://www.euclid-ec.org>

<sup>2</sup><https://www.lsst.org/>

inferring the mass within some radius, or by directly adding up the surface mass density—which can be obtained from the shear—within some aperture. Since we are only able to securely identify clusters above some threshold in the observed signal,  $\mathcal{O}_{\text{lim}}$ , a correct calibration of the mass–observable relation also requires the abundance of clusters to be taken into account. After all, the number of haloes around the detection limit will depend not only on the uncertainty in the mass–observable relation, but also on the expected number of haloes at that given mass (see Mantz, 2019 for a clear discussion of this effect).

A full cluster cosmology analysis then calibrates the cosmology- and redshift-dependent relations  $P(\mathcal{O}, z | \mathcal{M}_{\text{obs}}, \boldsymbol{\Omega}, \mathcal{S})$  and  $P(\mathcal{M}_{\text{obs}}, z | \mathcal{M}, \boldsymbol{\Omega}, \mathcal{S})$ , by fitting them jointly with the theoretical halo abundance,  $n(\mathcal{M}, z | \boldsymbol{\Omega}, \mathcal{S})$ , to the observed cluster number counts within bins  $\mathcal{O}_i$  and  $z_j$ ,  $N(\mathcal{O}_i, z_j)$ . The halo abundance possibly depends on the selection function for quality cuts based on the halo environment, for example to exclude chance alignments or mergers. We write out the forward model as

$$\begin{aligned} N(\mathcal{O}_i, z_j | \boldsymbol{\Omega}, \mathcal{S}) &= \Omega_{\text{sky}} \int_{\mathcal{O}_i}^{\mathcal{O}_{i+1}} d\mathcal{O} \int_{z_j}^{z_{j+1}} dz \frac{dV(z, \boldsymbol{\Omega})}{d\Omega dz} \int d\mathcal{M} d\mathcal{M}_{\text{obs}} \\ &\quad \times P(\mathcal{O}, z | \mathcal{M}_{\text{obs}}, \boldsymbol{\Omega}, \mathcal{S}) P(\mathcal{M}_{\text{obs}}, z | \mathcal{M}, \boldsymbol{\Omega}, \mathcal{S}) \\ &\quad \times n(\mathcal{M}, z | \boldsymbol{\Omega}, \mathcal{S}), \end{aligned} \quad (4.1)$$

where  $\mathcal{O}$  and  $z$  are integrated over their respective bins, and  $\mathcal{M}_{\text{obs}}$  and  $\mathcal{M}$  over all possible values. We convert the halo number density to the number counts taking into account the cosmology-dependent comoving volume at redshift  $z$ ,  $V(z, \boldsymbol{\Omega})$ , probed by a survey covering a solid angle  $\Omega_{\text{sky}}$ . Correctly modelling the cluster selection is of vital importance in any attempt to derive cosmological constraints from galaxy clusters. Ideally, we would detect clusters through an observable that has a straightforward selection function. Since the selection function depends on the survey under consideration, we will assume here that the selection has been modelled correctly. This simplifies the derivation of the main points we want to make.

Currently, cluster analyses infer 3D halo masses from weak lensing observations to determine the mass–observable relation (see e.g. Bocquet et al., 2020; DES Collaboration et al., 2020). The appeal of 3D halo masses stems from analytic arguments such as the (extended) Press-Schechter theory (Press & Schechter, 1974; Bond et al., 1991), that predict that the 3D halo mass function has a universal shape set only by the significance of the seed perturbation of a halo in the initial Gaussian density field. In recent years, however, ever larger suites of cosmological dark matter-only (DMO) simulations have shown that the assumed *universality* of the 3D halo mass function does not hold in detail. Simulated abundances can deviate from the universal prediction by > 10 per cent depending on the redshift and the exact cosmology (see e.g. Tinker et al., 2008; Bhattacharya et al., 2011; Despali et al., 2016; Diemer, 2020). Hence, suites of large-volume cosmological simulations run on a grid of different cosmological parameter values are vital to

capture the cosmology dependence of the halo mass function through either analytic fitting functions (Tinker et al., 2008; Bhattacharya et al., 2011) or emulators (McClintock et al., 2019; Nishimichi et al., 2019; Bocquet et al., 2020).

Problemsatically, 3D halo masses cannot be measured directly from observations, which first need to be deprojected. Generically, deprojection requires the assumption of a spherically symmetric density profile, which will be affected by baryons and scatter introduced by halo triaxiality, substructures, and correlated structures (see e.g. Becker & Kravtsov, 2011; Oguri & Hamana, 2011; Bahé et al., 2012; Henson et al., 2017; Debackere et al., 2021). This introduces model-dependent biases and increases the uncertainty in the inferred 3D halo masses, degrading the cosmological constraints from cluster cosmology. Note that this step is only required to transform the observations to theory predictions. As we argue in this paper, such a procedure is not necessary.

Since modern theoretical predictions for the halo abundance already rely on large simulation suites, it is possible to perform the cluster mass calibrations with halo properties that *can* be measured directly in both observations and simulations. This has the additional advantage that dark matter-only simulations can optionally be replaced by hydrodynamical simulations in order to account for baryonic effects on the halo mass function (e.g. Velliscig et al., 2014) or to directly predict a baryonic observable. We focus on weak lensing observations because they probe the total matter content and are thus less sensitive to uncertainties in how baryonic matter traces the dark matter. From the weak lensing shear signal we can directly measure projected aperture masses within apertures of a fixed angular or physical size, without the need to assume any density profile (see e.g. Schneider, 1996; Bartelmann & Schneider, 2001). Importantly, these aperture masses can also be measured directly in simulations.

Aperture masses have been studied before in the context of cluster cosmology with purely shear-selected samples in order to bypass uncertainties due to the selection based on some baryonic observable such as the X-ray luminosity, the SZ signal or the galaxy overdensity citep[e.g.][]reblinsky1999a. Marian et al. (2010) argued that future surveys would no longer need to convert shear peaks to 3D halo masses, if predictions for the halo abundance as a function of their aperture mass were available. However, Hennawi & Spergel (2005) showed that while almost all massive clusters produce significant aperture mass peaks, there is a large population of significant peaks that cannot be ascribed to a single cluster but rather is the result of chance superpositions along the line-of-sight due to the broad lensing kernel. Hence, to decrease the number of false-positive cluster detections, baryonic observables are still required for confirmation. More recently, Hamana et al. (2015), Shan et al. (2018) and Martinet et al. (2018) have used peaks identified from weak lensing observations to constrain the matter density and clustering of the Universe.

With the availability of large-volume simulation suites run for many different cosmological models, it is now possible to calibrate the cosmology dependence of the halo aperture mass function. Importantly, with aperture mass measurements the theoretical model assumptions separate cleanly from the purely observational

data in Eq. (4.1). That is, Eq. (4.1) splits into an observational scaling relation,  $P(\mathcal{O}, z | \mathcal{M}_{\text{obs}}, \boldsymbol{\Omega}, \mathcal{S})$ , independent of the cluster density profile, and a calibration between the observed and the simulated aperture mass measurement,  $P(\mathcal{M}_{\text{obs}}, z | \mathcal{M}, \boldsymbol{\Omega}, \mathcal{S})$ . The uncertainty in the observational scaling relation will depend on how accurately  $\mathcal{O}$  can be measured in the survey, and how strongly it correlates with the aperture mass. The theoretical calibration, on the other hand, will have a fixed uncertainty set by the shape noise of the observations, since the aperture mass measured from the weak lensing shear is an unbiased measure of the true aperture mass (Schneider, 1996). Moreover, as shown by Debackere et al. (2021), halo aperture masses are expected to be less sensitive to baryonic effects, especially when measured within larger apertures that are able to capture more of the ejected halo baryons. We study how baryons modify aperture mass measurements in Debackere et al. (2022).

Here, we investigate the behaviour of the different components that enter the model for the cluster number counts in Eq. (4.1), that is, the uncertainty in the mass–observable relation and the halo mass function for halo aperture masses. We will show that the mass–observable relation can be calibrated more precisely with aperture masses than with the standard deprojected 3D halo masses. Additionally, we will use an emulator calibrated on the Mira–Titan suite of large-volume cosmological N-body simulations to show that the halo aperture mass function is also highly sensitive to variations in the cosmological parameters, in agreement with Marian et al. (2010). This study serves as a proof-of-concept that can be applied in future cosmological analyses when carefully calibrated emulators for the halo aperture mass function are available.

The paper is structured as follows: first, we introduce the large-volume simulation suite that we use for our analysis in Section 4.2. Then, in Section 4.3, we study the dependence of the aperture mass on both the 3D halo mass and the aperture size, and use the clean separation between the theoretical and observational uncertainties in aperture mass measurements to study the behaviour of the mass–observable relation. In Section 4.4, we build an emulator to investigate the sensitivity of the aperture mass function to changes in the cosmological parameters, comparing it to the 3D halo mass function. We compare our analysis with the wider literature, discuss advantages and possible difficulties, and provide future applications in Section 4.5. Finally, we conclude in Section 4.6.

## 4.2 Simulations

We use the Mira–Titan suite of cosmological, gravity-only simulations, run with the HACC N-body code (Hardware/Hybrid Accelerated Cosmology Code, Habib et al. 2016). This simulation suite is well-suited to our purpose: it contains large-volume simulations with cosmological parameters sampled using a nested space-filling design that is ideal for interpolating the simulation predictions. The simulations include dynamical dark energy and massive neutrinos. The publically available data products of the simulation suite are described in more detail in

Table 4.1: Cosmological parameter values for the Mira–Titan suite of large-volume, cosmological N-body simulations.

Parameter	Min	Max
$\Omega_m h^2$	0.12	0.155
$\Omega_b h^2$	0.0215	0.235
$\Omega_\nu h^2$	0.0	0.01
$\sigma_8$	0.7	0.9
$h$	0.55	0.85
$n_s$	0.85	1.05
$w_0$	-1.3	-0.7
$w_b \equiv (-w_0 - w_a)^{1/4}$ <sup>†</sup>	0.3	1.3
$w_a$	-1.56	1.29

<sup>†</sup> Heitmann et al. (2016) show that this rescaling improves the prediction accuracy of cosmological models with  $w_0 + w_a \approx 0$  by putting slightly more points near the  $w_0 + w_a = 0$  boundary.

Heitmann et al. (2019). So far, Mira–Titan has been used to construct emulators for the matter power spectrum (Heitmann et al., 2016; Lawrence et al., 2017) and the 3D halo mass function (Bocquet et al., 2020).

The simulation suite consists of a grid of 111 simulations that vary 8 different cosmological parameters. The cosmological parameters are chosen according to a nested lattice design that enforces space-filling properties at multiple design steps (see Section 3 of Heitmann et al., 2016). This design works well with Gaussian process emulators and has an important global convergence property that allows systematic improvement of emulation accuracy as more design points are added. All cosmologies are spatially flat with  $\Omega_k = 0$ . The models vary the cosmological parameters within the ranges shown in Table 4.1. The full grid of cosmological parameters is shown in figure 1 of Bocquet et al. (2020).

The Mira–Titan suite consists of 3 nested tessellations that refine the higher level grids (M011–M036, M037–M065, and M066–M111, respectively). These models all include massive neutrinos. To enable accurate predictions for the Standard Model of cosmology with massless neutrinos, the simulation suite includes an additional 10 simulations with  $m_\nu = 0$  with the remaining 7 cosmological parameters sampled on a symmetric Latin hypercube (M001–M010). All simulations have box sizes of 2.1 Gpc (except for M006, M023, and M046 with 2.091, 2.085, and 1.865 Gpc, respectively) and include  $3200^3$  particles with masses  $m_{dm} = 7.23 \times 10^9 - 1.22 \times 10^{10} M_\odot$  depending on the cosmology. Hence, groups and clusters with  $m > 10^{13} M_\odot$  are generally resolved with  $> 1000$  particles. All simulations use a force softening length of  $\epsilon = 6.6$  kpc. For our analysis, we focus on the 100 simulations with massive neutrinos (M011–M110, for the distribution of the cosmological parameters, see fig. 1 of Bocquet et al. 2020).

We now briefly describe how dynamical dark energy and massive neutrinos are included in the simulations, referring to Upadhye et al. (2014) and Heitmann et al. (2016) for the full details. Both massive neutrinos and dynamical dark

energy are included at the level of the background evolution,  $H(z)$ , and the initial conditions. Particularly, the linear  $z = 0$  transfer function includes dark matter, baryons, and massive neutrinos and is normalized to the correct  $\sigma_8$ . Then, the matter component including dark matter and baryons is evolved back to the initial redshift assuming a scale-independent growth factor including all species in the homogeneous background and used to determine the initial particle positions and velocities. This ensures that the  $z = 0$  linear power spectrum of the simulation is correct on large scales. For power spectrum calculations, the neutrino contribution needs to be included by hand. Hence, the simulations do not account for neutrino clustering, which is no cause for concern, since this effect is much smaller than the suppression of the halo mass function due to neutrino free-streaming for the neutrino mass range considered.

The saved simulation data products had to be chosen carefully due to the large volume of the simulations and the size of the cosmological parameter hypercube. For each simulation output, the full particle data is downsampled by a factor 100 before saving. Simulation haloes are identified on the fly, i.e. from the full particle data, using a friends-of-friends (FoF) algorithm with linking length  $b = 0.168$ . Subsequently, spherical overdensity masses, defined as  $m_{\Delta c} = 4/3\pi\Delta\rho_{\text{crit}}(z)r_{\Delta c}^3$ , with overdensity  $\Delta = 200$  are determined around the potential minimum of the FoF halo. For all haloes with  $> 1000$  particles (corresponding to  $m_{\text{FoF}} \gtrsim 10^{13} M_\odot$ ), all the particles belonging to the FoF halo are also saved separately. We will use the downsampled particle catalogues to compute the projected aperture masses around the identified FoF haloes with spherical overdensity masses  $m_{200c} > m_{200c,\text{lim}} = 10^{13.5} M_\odot$ . In Fig. 4.2 and Section 4.3.1, we show that the Poisson noise due to the downsampling introduces an uncertainty of  $> 15$  per cent in the measured aperture masses of haloes with  $m_{200c} < 10^{14} M_\odot$ . Hence, we will mainly focus on haloes with  $m_{200c} > 10^{14} M_\odot$  in the rest of this paper.

### 4.3 Aperture mass–observable relation

To quantify the uncertainties in the aperture mass–observable relation, we first need to measure the halo aperture masses. In Section 4.3.1, we describe how we extract the halo aperture masses from the Mira–Titan suite. We show how halo aperture masses depend on the 3D halo mass and the aperture size in Section 4.3.2. Finally, we investigate the possible theoretical and observational uncertainties in the aperture mass–observable relation and compare our results to 3D halo masses in Section 4.3.3.

### 4.3.1 Extraction from the simulations

We will use the term aperture mass, in accordance with the literature, to refer to the projected mass difference

$$\begin{aligned}\Delta M(< R_1 | R_2, R_m) &= \pi R_1^2 (\bar{\Sigma}(\leq R_1) - \bar{\Sigma}(R_2 < R \leq R_m)) \\ &= M(\leq R_1) - M_{\text{bg}}(\leq R_1),\end{aligned}\quad (4.2)$$

where we have introduced the mean enclosed surface mass density,  $\bar{\Sigma}$ , which is defined as

$$\bar{\Sigma}(R_2 < R \leq R_m) = \frac{2}{R_m^2 - R_2^2} \int_{R_2 < R < R_m} dR R \Sigma(R). \quad (4.3)$$

The second term in Eq. (4.2) corrects the mass within the aperture  $R_1$  for the average surface mass density within the control annulus bounded by  $R_2$  and  $R_m$ , which acts as a local background subtraction,  $M_{\text{bg}}$ . Both terms get the same contribution from the mean cosmological background density along the line-of-sight, which cancels out in the difference. The background subtraction makes the aperture mass independent of the line-of-sight integration length, provided it is large compared with the clustering length (as also noted by Marian et al., 2010). We verify this below.

The power of the aperture mass defined in Eq. (4.2) is that it can be obtained directly from weak lensing observations, as shown in Eq. (4.25) in Appendix 4.A. Moreover, choosing fixed physical or angular aperture sizes removes the need to assume a cluster density profile, in contrast to spherical overdensity radii. We will measure aperture masses within three different but fixed apertures of  $R_1 = [0.5, 1.0, 1.5] \text{ cMpc}$ , with  $R_2 = 2.0 \text{ cMpc}$  and  $R_m = 3.0 \text{ cMpc}$ . These apertures are similar to the typical aperture sizes used in weak lensing cluster mass calibrations (e.g. Hoekstra et al., 2015; Applegate et al., 2014). Moreover, they also roughly correspond to the halo radii for haloes with  $m_{200c} > 10^{13} M_\odot$ . Smaller apertures will give better signal-to-noise ratios (SNRs) for lower-mass haloes since they are better matched to their sizes (Schneider, 1996). To compare these results with aperture masses inferred from observations, the distances in the simulations need to be converted into angular positions,  $\theta$ , using the angular diameter distance to the lens for the simulated cosmology.

Since the aperture mass from weak lensing observations is inferred from the shear signal within the annulus between  $R_1$  and  $R_m$ , the optimal choice of the aperture sizes balances the increased signal from decreasing  $R_1$  and increasing  $R_m$ , respectively, against the increased modelling uncertainty due to contamination from cluster member galaxies and miscentring errors, and the contribution of cosmic noise in the cluster outskirts (e.g. Mandelbaum et al., 2010). We stress that the aperture mass in Eq. (4.2) will be computed directly from the simulation data without any assumptions about the weak lensing observations. Any observational uncertainty in converting the weak lensing signal to the surface mass density will thus be included in the  $P(\Delta M_{\text{obs}} | \Delta M, z)$  term in Eq. (4.1), leaving

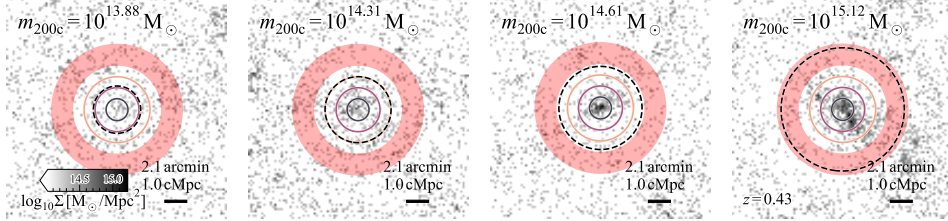


Figure 4.1: Surface mass density maps for randomly selected haloes in mass bins  $\log_{10} m_{200c}/M_\odot \in [13.5, 14.0, 14.5, 15, 15.5]$  for simulation M000 at  $z = 0.43$ . Each cutout has size  $10 \text{ cMpc} \times 10 \text{ cMpc}$  and is plotted on the same colour scale. The dashed circles indicate the spherical overdensity radius  $r_{200c}$  for each halo. With the coloured lines, we show the inner apertures  $R_1 = [0.5, 1.0, 1.5] \text{ cMpc}$  which we use throughout this work. The red shaded region shows the outer control annulus between  $R_2 = 2.0 \text{ cMpc}$  and  $R_m = 3.0 \text{ cMpc}$  for the background subtraction.

the aperture mass function unaffected. We discuss such observational uncertainties in Section 4.3.3. In practice, the observed weak lensing aperture mass includes the contribution of mass along the line-of-sight, weighted by the lensing kernel. However, as we will show in Fig. 4.3, the total aperture mass is dominated by the correlated structure within  $\approx 30 \text{ cMpc}$  of the cluster, which justifies neglecting the lensing kernel weighting in our analysis.

Given the downsampled particle catalogue, calculating halo aperture masses is relatively straightforward. First, we correct the particle catalogues for the downsampling (see Section 4.2) by increasing the particle masses by a factor 100. We investigate the effect of this downsampling on the accuracy of the derived halo masses below. We generate projected maps of the surface mass density,  $\Sigma$ , along the three principal axes of the simulation volume on a grid of  $21000 \times 21000$  pixels, corresponding to a pixel size of  $(L/21000)^2 = (0.1 \text{ cMpc})^2$  (except for the simulations with smaller box sizes). Subsequently, we can directly obtain halo aperture masses from the surface mass density maps by calculating Eq. (4.2) centred on the identified halo centres.

In Fig. 4.1, we show the surface mass density maps centred on 4 random haloes within mass bins with bin edges specified by  $\log_{10} m_{200c}/M_\odot \in [13.5, 14.0, 14.5, 15.0, 15.5]$  for reference simulation M000 at  $z = 0.43$ . Clearly, the downsampling of the particle catalogue results in emptier and noisier mass maps. Every particle in the simulation has a  $p = 0.01$  chance of being included in the downsampled particle catalogue. As a result, particle catalogues of downsampled haloes will include a shot-noise contribution of  $pN$ , resulting in a fractional uncertainty on the final 3D halo mass of  $\delta m/m = \sqrt{pN}^{-1}$ , which is  $\approx [20, 10, 6, 3, 2]$  per cent for haloes located at the mass bin edges. Since the spherical overdensity halo masses were saved on the fly, the downsampling does not affect the halo mass catalogues. The aperture masses, however, are affected by the particle downsampling. We show the distribution of the fractional aperture mass uncertainty due to the finite number

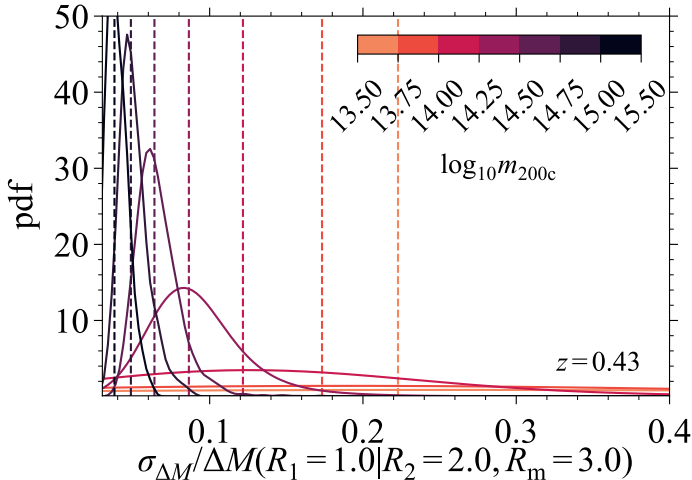


Figure 4.2: Distribution of the uncertainty in the aperture mass, given in Eq. (4.2), for different 3D halo mass bins due to the factor of 100 downsampling of the saved simulation particle catalogues. We add the Poisson uncertainties of the downsampled number of simulation particles within  $R < R_1 = 1.0 \text{ cMpc}$  and  $R_2 \leq R < R_m$  in quadrature for all haloes with  $m_{200c} > 10^{13.5} \text{ M}_\odot$  in M000 at  $z = 0.43$ . Different coloured lines correspond to different 3D halo mass bins and the dashed lines indicate the median uncertainty. The downsampling results in a significant uncertainty in the derived aperture masses for haloes with  $m_{200c} < 10^{14.25} \text{ M}_\odot$ .

4

of particles for different 3D halo mass bins in Fig. 4.2. We show the fractional uncertainty,  $\sigma_{\log \Delta M} = \sigma_{\Delta M}/\Delta M$ , for  $R_1 = 1.0 \text{ cMpc}$ , since this aperture size is similar to the virial radius for haloes with  $10^{13.5} < m_{200c}/\text{M}_\odot < 10^{14}$ . We calculate the uncertainty by adding the shot noise contributions to  $M(< R_1)$  and  $M_{\text{bg}}(< R_1)$  in quadrature. Even though the individual contributions to the aperture mass in Eq. (4.2) can be determined at high accuracy due to the extra particles included along the line-of-sight, their difference has a large fractional uncertainty. Hence, we will limit our halo sample to haloes with  $m_{200c} > 10^{14} \text{ M}_\odot$  whose aperture masses can be determined with a median fractional uncertainty of  $\lesssim 15$  per cent from the available particle data. We note that even though the median uncertainty of the mass bin  $10^{14.0} < m_{200c}/\text{M}_\odot < 10^{14.25}$  is  $\lesssim 15$  per cent, there are also significant outliers.

It is important to verify that the background subtraction in the aperture mass definition, Eq. (4.2), actually makes the aperture mass independent of the line-of-sight integration depth. In Fig. 4.3, we show the calculated aperture masses as a function of the line-of-sight integration length,  $L$ , centred on 10000 random positions (first column) or on all haloes within different halo mass bins that have  $x$ -coordinates that are within  $\pm 5 \text{ cMpc}$  of the midpoint of the  $x$ -axis of the simulation box (second to fourth columns) for simulation M000 at  $z = 0.43$ . When centring on

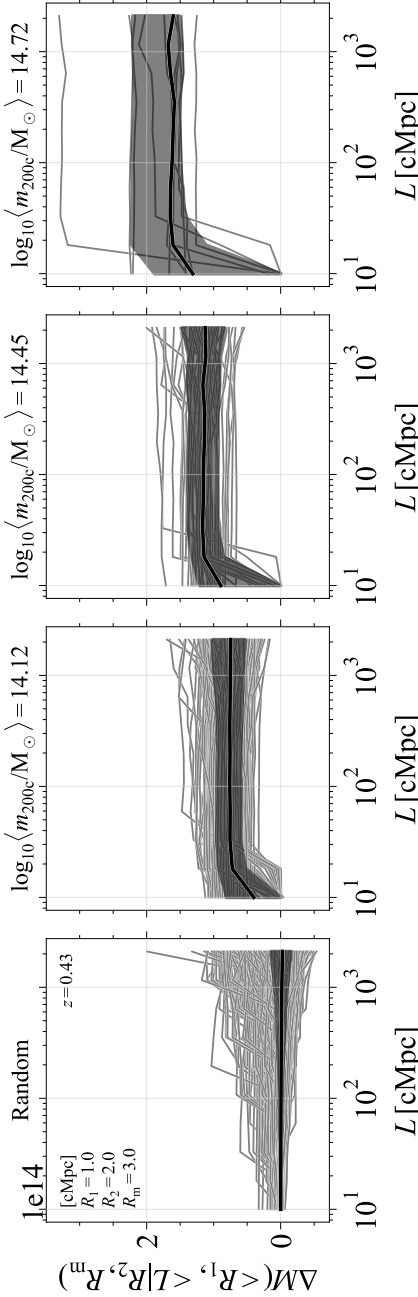


Figure 4.3: Convergence of the aperture mass,  $\Delta M$ , with the line-of-sight depth,  $L$ , centred on random positions (*first column*), and haloes within increasing  $m_{200c}$  bins (*second to fourth columns*). Light grey lines indicate the individual positions/haloes, which were chosen to have  $x$ -coordinates within  $\pm 5$  cMpc of the centre of the  $x$ -axis along which we project. The median and 16th to 84th percentile scatter are indicated with thick black lines and the shaded region, respectively. The median aperture mass along random lines-of-sight is zero, as expected, with a slight increase in the scatter for larger line-of-sight integration lengths. Lines-of-sight centred on haloes generally converge within  $\approx 30$  cMpc along the line-of-sight, with a large scatter that increases slightly with increasing  $L$ . The aperture mass for individual haloes can increase or decrease significantly when encountering a massive structure along the line-of-sight within  $R_1$  or  $R_2 < R_m$ , respectively.

random positions, the aperture masses are consistent with zero since the average surface mass densities within  $R_1$  and the control annulus are equal. The scatter in the aperture masses for randomly-positioned apertures, which is equivalent to measuring the cosmic shear on the scale of the aperture, increases with the line-of-sight integration depth, since larger modes contribute to the dispersion  $\langle \Delta M^2(< R_1, < L|R_2, R_m) \rangle$  (see e.g. Schneider et al., 1998). This effect is also present when centring on haloes, but since the cosmic shear introduces a fixed scatter, the effect is relatively smaller for more massive haloes (Hoekstra, 2001). For haloes, the average aperture mass generally converges to its final value within  $\approx 30$  cMpc. However, the individual halo trajectories along the line-of-sight can increase or decrease significantly when encountering massive structures within  $R_1$  or  $R_2 < R < R_m$ , respectively. Hence, we confirm that the aperture mass measurements are converged with respect to the line-of-sight integration length of  $L = 2100$  cMpc.

The aperture mass measurements in the simulations automatically include the intrinsic scatter due to halo triaxiality and substructure, and due to both correlated and uncorrelated large-scale structures. We do not include observational uncertainties since these will depend on the survey of interest. One source of observational systematic uncertainty is the shear map generation, which relies on the accuracy of the shape measurements of the background source galaxies and the determination of their redshift distribution (e.g. Von der Linden et al., 2014; Hoekstra et al., 2015). Another source of uncertainty is the centring of the aperture on the halo. In the simulations, we centre the surface mass density maps exactly on the potential minimum of the spherical overdensity, but observationally this centre cannot be identified so unambiguously. However, Hoekstra et al. (2012) showed that deprojected mass estimates derived from aperture mass measurements within large apertures corresponding to overdensity radii with  $\Delta < 1000$ , are only affected by  $\lesssim 5$  per cent for miscentring radii up to  $0.5 h_{70}^{-1}$  cMpc. For reference, the distribution of the offset,  $\Delta R$ , between the SZ signal peak and the location of the brightest cluster galaxy position shows that the bulk of clusters ( $\approx 95$  per cent) are well centred with  $\sigma_{\Delta R} \lesssim 0.2 R_{500c}$ , which is smaller than  $0.5 h_{70}^{-1}$  cMpc for all clusters with  $m_{500c} \lesssim 5 \times 10^{15} M_\odot$ , while the remaining clusters show a larger dispersion  $\sigma_{\Delta R} \approx 0.7 R_{500c}$  (see e.g. Saro et al., 2015; Bleem et al., 2020). In the same vein as the results of Hoekstra et al. (2012), aperture masses measured within apertures considerably larger than the miscentring radius of the cluster should not be significantly affected by miscentring. Hence, ignoring miscentring does not change the conclusions of our work. Next, we will show the dependence of halo aperture masses on the 3D halo mass and the aperture.

### 4.3.2 Aperture mass behaviour

Since halo properties are mostly studied as a function of their 3D mass, we show the distribution of aperture masses for  $R_1 = 1.0$  cMpc,  $R_2 = 2$  cMpc, and  $R_m = 3$  cMpc as a function of the 3D halo mass,  $m_{200c}$ , at  $z = 0.43$  in the M011 simulation in the top panel of Fig. 4.4. The median  $\Delta M$ – $m_{200c}$  relation, indicated with the solid line, is slightly shallower than one-to-one: the aperture mass for haloes with

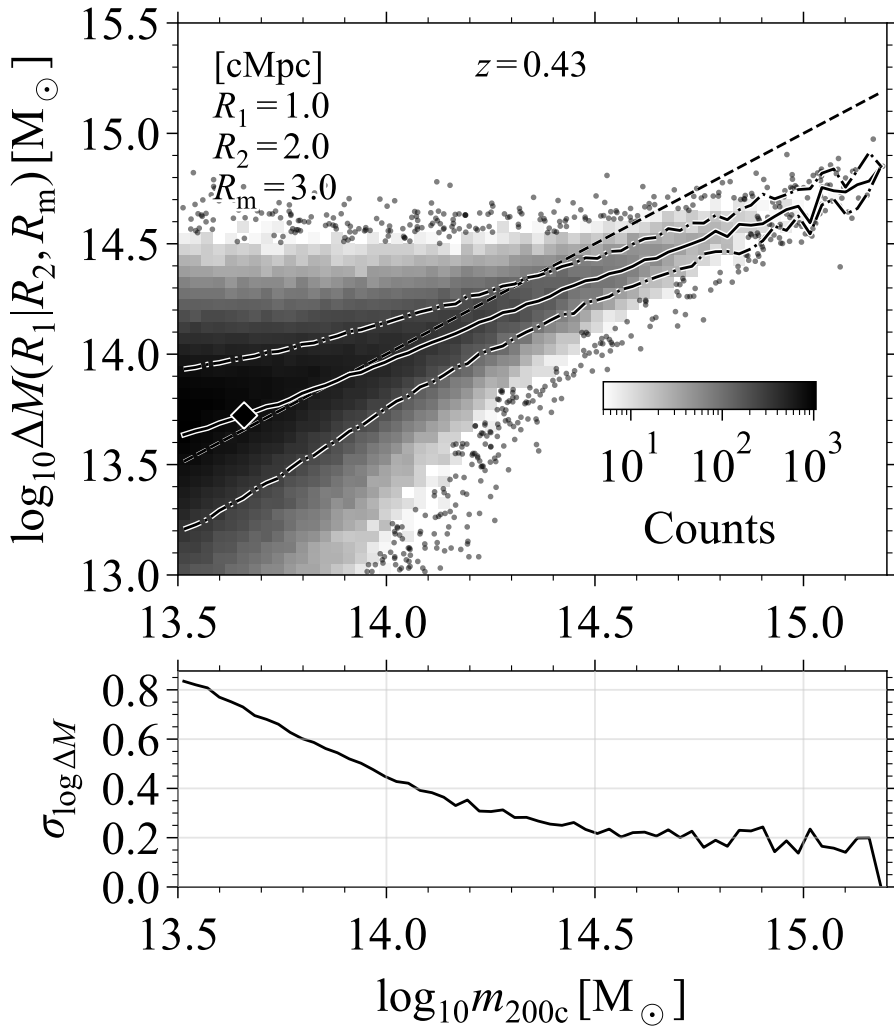


Figure 4.4: *Top panel:* The distribution of aperture masses,  $\Delta M(< R_1 = 1.0 \text{ cMpc} | R_2 = 2.0 \text{ cMpc}, R_m = 3.0 \text{ cMpc})$ , as a function of the 3D spherical overdensity mass  $m_{200c}$  for simulation M011 at  $z = 0.43$ . The dashed line indicates the one-to-one relation, the solid line indicates the median relation, and the dash-dotted lines the 16th and 84th percentile scatter. The diamond indicates the 3D halo mass for which  $r_{200c} = R_1$ . The large scatter in  $\Delta M$  at fixed  $m_{200c}$  is caused by the large variation in the matter distribution along the line-of-sight. *Bottom panel:* The logarithmic scatter in the aperture mass distribution at fixed  $m_{200c}$ , calculated as half the difference between the 84th and the 16th percentiles. The scatter decreases from  $\sigma_{\log \Delta M} \approx 0.45$  at  $m_{200c} = 10^{14} \text{ M}_\odot$  to  $\lesssim 0.2$  for  $m_{200c} > 10^{14.5} \text{ M}_\odot$ .

$r_{200c} \gtrsim (\lesssim) R_1$  is smaller (larger) than  $m_{200c}$  since the halo mass represents a larger (smaller) fraction of the total aperture mass. For simulation M011, the halo radius  $r_{200c} = R_1 = 1.0 \text{ cMpc}$  for  $m_{200c} \approx 10^{13.65} \text{ M}_\odot$ . Haloes at fixed  $m_{200c}$  can have greatly differing aperture masses due to differences in the matter distribution along the line-of-sight of haloes at fixed 3D mass (see also Fig. 4.3). For low-mass haloes the scatter around the median relation increases significantly since mass outside the halo contributes relatively more to the mass within the aperture.

In the bottom panel of Fig. 4.4, we show the logarithmic scatter around the median  $\Delta M - m_{200c}$  relation. We calculate the scatter as half the difference between the 84th and the 16th percentile of  $\log \Delta M$ . The scatter increases strongly for low-mass haloes, partially due to the particle downsampling of the halo catalogues shown in Fig. 4.2, but also since matter outside the halo contributes more to the aperture mass. The intrinsic scatter in the aperture mass at fixed halo mass decreases from  $\sigma_{\log \Delta M} \approx 0.45$  for  $m_{200c} = 10^{14} \text{ M}_\odot$  to  $\lesssim 0.2$  for  $m_{200c} > 10^{14.5} \text{ M}_\odot$ , which is similar to the scatter in the weak lensing-inferred 3D halo mass at fixed halo mass due to triaxiality and substructure (see Fig. 4.7 and Section 4.3.3 for a comparison with the mock weak lensing analysis from Bahé et al. 2012). The scatter at high halo masses is dominated by differences in the projected structure along the line-of-sight to the halo, both correlated and uncorrelated, since the downsampling has a negligible effect on high-mass haloes.

## 4

Since different apertures are naturally tuned to detect haloes of different mass and size, we show the median relation between the aperture mass,  $\Delta M$ , measured in different apertures and the 3D halo mass,  $m_{200c}$ , for all cosmologies in the hypercube in the left panel of Fig. 4.5. Smaller apertures more closely capture the 3D mass of lower-mass haloes, however, as is clear from Fig. 4.4, there is a large scatter around the median relation due to the differing matter distributions along the line-of-sight to different haloes. For higher-mass haloes, measuring the mass in different apertures allows the characterization of the halo density profile, since the matter belonging to the halo dominates the total aperture mass out to larger apertures.

In the right-hand panel of Fig. 4.5, we show the redshift evolution of the aperture mass within a fixed aperture of  $R_1 = 1 \text{ cMpc}$ . Since we measure within fixed comoving apertures, the uncorrelated large-scale structure contribution to both  $M(< R_1)$  and  $M_{\text{bg}}(< R_1)$  should be the same on average. Hence, the redshift evolution is dominated by the local overdensity changes around the halo. At fixed  $m_{200c}$ , the virial radius  $r_{200c}$  will increase less rapidly with increasing time than the aperture radius does as the critical density—and also  $r_{200c}(z)$ —approaches a constant in the dark energy-dominated era. As a result, the aperture mass increases with time, since more matter outside of the halo is included within the same comoving aperture at fixed halo mass. For angular apertures, there would be an additional change due to the changing angular diameter distance. For a halo mass defined with respect to the mean matter density, such as  $m_{200m}$ , the virial radius and the comoving aperture radius do not evolve with redshift at fixed halo mass and, hence, the redshift evolution would be set by the change in the halo density profile.

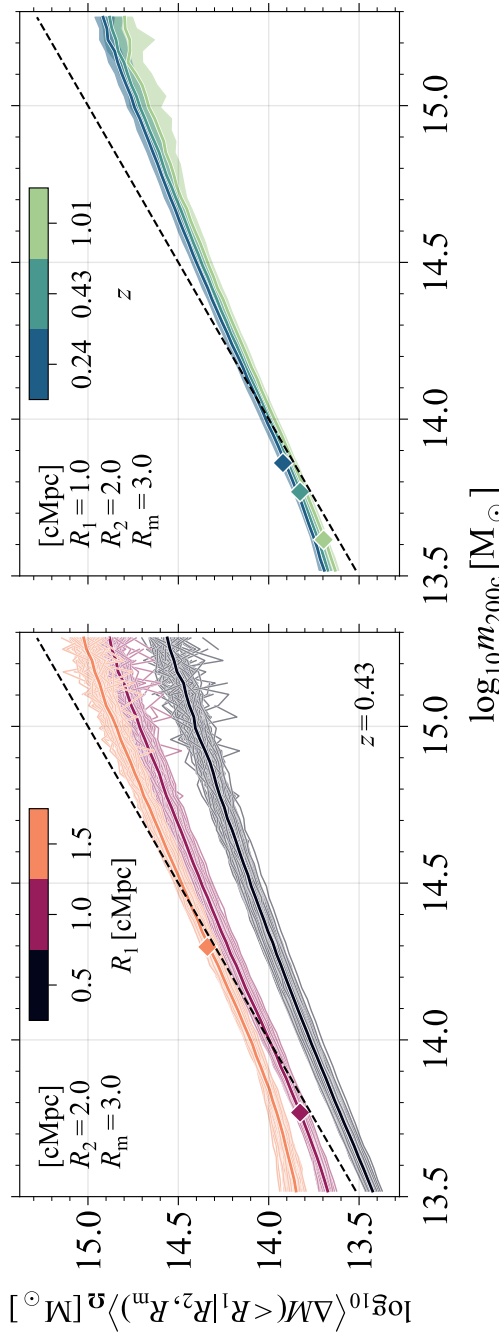


Figure 4.5: *Left panel:* The relation between the median projected aperture masses of all cosmologies in the hypercube,  $\langle \Delta M(< R_1 | R_2, R_m) \rangle_\Omega$ , within different apertures  $R_1$  (thick coloured lines) and the 3D spherical overdensity mass  $m_{200c}$ . The thin, transparent lines show the results for individual simulations. The black, dashed line indicates the one-to-one relation. The coloured diamonds show the halo mass for which  $r_{200c} = R_1$ . The reference annulus for all aperture mass measurements spans the region between  $R_2 = 2$  cMpc and  $R_m = 3$  cMpc. Masses measured within larger apertures more closely match the 3D masses of more massive haloes. *Right panel:* The redshift evolution of the relation between the median aperture mass of all cosmologies and  $m_{200c}$ . At fixed  $m_{200c}$ , the ratio of the virial radius,  $r_{200c}$  and the comoving aperture radius decreases with time due to increasing contribution of dark energy to the critical density. The extra contribution of the halo outskirts within the fixed comoving aperture increases the measured aperture masses with time.

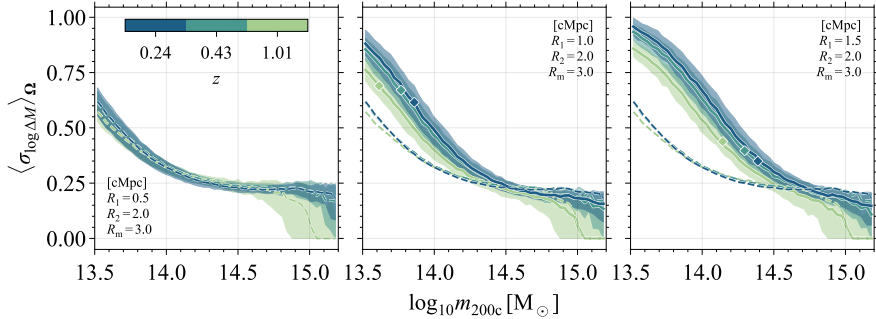


Figure 4.6: The median redshift evolution of the scatter in the  $\Delta M - m_{200c}$  distribution measured in apertures  $R_1 \in [0.5, 1.0, 1.5]$  cMpc for all simulations (*left to right columns*). Coloured lines and shaded regions indicate the median and the 16th to 84th percentile scatter for all cosmologies at different redshifts. The  $R_1 = 0.5$  cMpc distribution is indicated with dashed lines and repeated in the other panels. The coloured diamonds show the median halo mass for which  $r_{200c} = R_1$  (these masses are smaller than  $10^{14} M_\odot$  for  $R_1 < 1.5$  cMpc). At fixed  $m_{200c}$  and  $R_1$ , the scatter increases significantly with time for haloes whose virial radius,  $r_{200c}$ , is not significantly larger than the aperture (low-mass haloes) or whose number density increases (high-mass haloes). Increasing  $R_1$  at fixed  $m_{200c}$  increases the scatter when the virial radius becomes comparable to the aperture due to the increased sensitivity to matter outside the halo.

4

To study how the scatter in  $\Delta M$  at fixed  $m_{200c}$  changes with cosmology and redshift, we show the redshift evolution of the median scatter,  $\sigma_{\log \Delta M}$ , of all cosmologies in the Mira–Titan suite for the different apertures in the panels of Fig. 4.6. The shaded regions show the 16th to 84th percentile scatter. We indicate the median halo mass for which  $r_{200c} = R_1$  with a coloured diamond. The overall trends are the same as in the bottom panel of Fig. 4.4, i.e. less scatter for higher-mass haloes. Within the smallest aperture,  $R_1 = 0.5$  cMpc, there is very little redshift evolution: the aperture is significantly smaller than  $r_{200c}$  for all halo masses shown, and the halo matter dominates the aperture mass. For all apertures, the increase in the scatter with time for the most massive haloes results mainly from their increasing number density with time. For the most massive haloes, the scatter only changes by  $\approx \pm 5$  per cent for different aperture sizes, as can be seen by comparing the dashed lines (which are for  $R_1 = 0.5$  cMpc in every panel) with the results for larger apertures in the middle and rightmost panels of Fig. 4.6. For lower-mass haloes, however, the scatter is more sensitive to the aperture and increases when the halo radius becomes comparable to the aperture.

So far, we have shown that aperture masses can be measured easily in simulations and that they correlate strongly with the true, 3D halo mass, albeit with a large intrinsic scatter due to their sensitivity to the matter along the line-of-sight to the halo. Paradoxically, this could give the aperture mass an advantage in the context of cluster cosmology since it means that the line-of-sight structure con-

tributes to the aperture mass signal, not its noise. We will investigate the possible strengths and difficulties of aperture mass calibrations for cluster cosmology next.

### 4.3.3 Uncertainties

For cluster cosmology, it is crucial that cluster masses inferred from observations can be calibrated accurately, that is without bias and, ideally, also with small uncertainties. Due to the exponential sensitivity of the halo abundance to the halo mass, biases and uncertainties that are not accounted for in the cluster mass measurement can introduce catastrophic biases in the inferred cosmological parameters. Consequently, minimizing the uncertainty in the mass–observable relation can dramatically increase the constraining power of cluster surveys. Previously, we have shown that the intrinsic scatter between the aperture mass and the 3D halo mass can be large, particularly for low-mass haloes. We will now consider the strengths and the difficulties of aperture masses for cluster cosmology.

Taking Eq. (4.1) as our guide, we see that the uncertainty in the mass–observable relation is due to the uncertainty in the relation between the measured observable and the measured aperture mass,  $P(\mathcal{O}|\mathcal{M}_{\text{obs}})$ , and the observational uncertainty between the measured aperture mass and the true halo aperture mass,  $P(\mathcal{M}_{\text{obs}}|\mathcal{M})$ , sometimes referred to in the literature as the intrinsic uncertainty (e.g. Becker & Kravtsov, 2011). First, we will look into the intrinsic measurement uncertainty of the halo aperture mass, comparing it to that of 3D halo masses.

The stringent requirements on the accuracy of the shear measurements for future surveys mean that the finite number of background galaxies used to sample the shear field and the source redshift distribution set the baseline, minimum uncertainty for any weak lensing mass measurement (e.g. Köhlinger et al., 2015). The source redshift distribution determines the critical surface mass density that enables the conversion from measured weak lensing shear to surface mass density. This uncertainty will affect any weak lensing mass measurement similarly, so we do not include it here. The uncertainty of aperture mass measurements is then fully determined by the galaxy shape noise, as shown by Schneider (1996). In comparison, 3D halo masses inferred from deprojected weak lensing observations are intrinsically highly sensitive to the large variation in the line-of-sight matter distribution at fixed, true 3D halo mass.

To quantify the intrinsic measurement uncertainties for 3D halo masses of individual clusters, we look at the literature. Bahé et al. (2012) have estimated the uncertainty of the  $P(\mathcal{M}_{\text{obs}}|\mathcal{M})$  scaling relation by generating mock weak lensing observations of clusters with  $m_{200c} > 10^{14} M_{\odot}$  at  $z \approx 0.2$ , a shape noise of  $\sigma_{\text{gal}} = 0.2$ , and with a mean lensed background galaxy number density  $\bar{n}_{\text{gal}} = 30 \text{ arcmin}^{-2}$  for sources at  $z = 1$ . This set-up assumes perfect knowledge of the source redshift distribution and the critical surface mass density. They find a large uncertainty of  $\sigma_{\log m_{\text{obs}}} = 0.45 (0.25)$  for haloes with  $m_{200c} = 10^{14} (10^{15}) M_{\odot}$  when inferring  $m_{\text{obs}}$  from fitting NFW density profiles to the observed lensing shear. Importantly, Bahé et al. (2012) only include the local, correlated large-scale structure within 10 cMpc of the halo when generating the lensing signal. However, uncorrelated

large-scale structures add to the scatter of the true lensing signal (e.g. Hoekstra, 2001, 2003). Hence, their results should be considered a lower limit on the true scatter in the inferred 3D halo masses. Becker & Kravtsov (2011) similarly find an uncertainty of  $\sigma_{\log m_{\text{obs}}} \approx 0.3$  for a mock sample with  $m_{200c} > 10^{14.5} h^{-1} M_{\odot}$  that does include the cosmic noise due to uncorrelated large-scale structure.

On the other hand, for the same set-up as Bahé et al. (2012), weak lensing aperture masses are only affected by the shape noise due to the finite number of galaxies used to sample the shear field. More specifically, the uncertainty is given by Eq. (4.21) in Appendix 4.A. We derive a fixed uncertainty  $\sigma_{\Delta M_{\text{obs}}} = 1.16 \times 10^{13} M_{\odot}$  for  $R_1 = 0.5 \text{ cMpc}$ ,  $R_2 = 2 \text{ cMpc}$ , and  $R_m = 3 \text{ cMpc}$ . For reference, from Fig. 4.5 we see that  $\Delta M(m_{200c} = 10^{14} M_{\odot}, R_1 = 0.5 \text{ cMpc}) \approx 10^{13.75} M_{\odot}$ , implying a fractional uncertainty  $\sigma_{\log \Delta M_{\text{obs}}} \approx 0.2$ , i.e. more than 2 times smaller than the fractional uncertainty in the 3D mass and without any dependence on an assumed density profile. Importantly, the fractional uncertainty scales inversely with the halo aperture mass, giving fractional uncertainties of  $\approx 0.1$  and  $0.05$  for  $\Delta M/M_{\odot} = 10^{14}$  and  $10^{14.5}$ , respectively.

In Fig. 4.7, we show the aperture radius dependence of the median fractional observational uncertainty,  $\sigma_{\log \Delta M_{\text{obs}}}$ , at fixed halo mass,  $m_{200c}$ , calculated from Eq. (4.21), for a lensing cluster at  $z = 0.24$  and source galaxies at  $z = 1$  with background density  $n_{\text{gal}} = 30 \text{ arcmin}^{-2}$  and shape noise  $\sigma_{\text{gal}} = 0.2$ , similar to Bahé et al. (2012). The aperture mass uncertainty in Eq. (4.21) additionally depends on the chosen filter, that is the aperture radii  $R_1$ ,  $R_2$ , and  $R_m$ . To obtain the fractional uncertainty, we divide  $\sigma_{\Delta M_{\text{obs}}}$  from Eq. (4.21) by the aperture mass,  $\Delta M$ . For  $R_1 = 1 \text{ cMpc}$ , we indicate the median uncertainty in the aperture mass at fixed  $m_{200c}$  over all cosmologies (the solid line in the middle panel of Fig. 4.6) as the shaded region. For comparison, we show the observational uncertainty in 3D halo masses inferred from the mock weak lensing observations of Bahé et al. (2012). Over the entire halo mass range, the aperture mass can be determined at least 2 times more precisely than the 3D halo mass for apertures similar to the halo radius. Increasing the inner aperture radius,  $R_1$ , increases the observational uncertainty since the weak lensing signal is inferred from the smaller number of galaxies within  $R_1$  and  $R_m$ . Hence, aperture masses can be measured more cleanly from observations than 3D halo masses since the line-of-sight structure contributes to the signal as opposed to the noise.

The uncertainty in aperture mass calibrations for cluster surveys with baryonic observables, such as the galaxy overdensity, the SZ signal or the X-ray luminosity, will also depend on the relation between the observable,  $\mathcal{O}$ , and the measured aperture mass,  $\Delta M_{\text{obs}}$ . As mentioned before, this relation depends solely on observational properties of the clusters and the uncertainty will be highly sensitive to the observable  $\mathcal{O}$  under consideration.

A particularly ill-suited scenario for aperture masses would be an observable that is not sensitive to projection effects, such as the X-ray luminosity or the thermal energy of the hot gas,  $Y_X$ . These observables depend strongly on the gas density and predominantly trace the cluster core. Due to the tight correlation with small scatter between the X-ray luminosity and the 3D halo mass,  $m$ , the

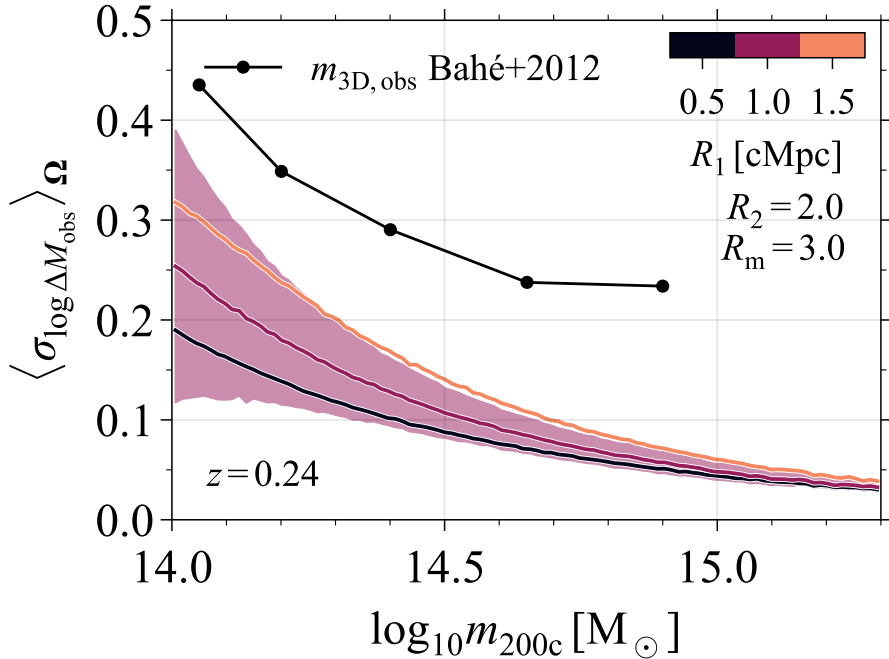


Figure 4.7: The median observational fractional uncertainty in the aperture mass at fixed halo mass within different apertures for a lensing cluster at  $z = 0.24$  and source galaxies at  $z = 1$  with a mean background density of  $\bar{n}_{\text{gal}} = 30 \text{ arcmin}^{-2}$  and shape noise  $\sigma_{\text{gal}} = 0.2$ . The thick, coloured lines indicate the median uncertainty over all cosmologies for  $m_{200c}$  and within different apertures. The shaded region shows the variation of the observational uncertainty for  $R_1 = 1 \text{ cMpc}$  due to the median scatter in  $\Delta M$  at fixed  $m_{200c}$  for all cosmologies, shown in Fig. 4.6. The black points show the scatter in the 3D masses inferred from mock weak lensing observations by Bahé et al. (2012). Smaller apertures have a lower observational uncertainty due to the larger number of background galaxies as the masses are measured within  $R_1 < R \leq R_m$ . Aperture masses can be determined more precisely than 3D masses over the full halo mass range.

uncertainty in  $P(\mathcal{O}|\Delta M_{\text{obs}})$  can be approximated by  $P(m|\Delta M_{\text{obs}})$ . As can be seen from the spread in  $m_{200c}$  at fixed  $\Delta M$  in the top panel of Fig. 4.4, this uncertainty is considerable. Such an observable is ideal for 3D halo mass calibrations. However, the uncertainty between the observable,  $\mathcal{O}$ , and the true halo mass,  $m$ , will still be limited by the uncertainty floor in  $P(m_{\text{obs}}|m)$ , set by the deprojection of the lensing profile.

In the best-case scenario for aperture masses, the observable closely traces the total projected mass with small uncertainty. Andreon & Congdon (2014) show that the richness is such an observable when measured within the same aperture as the weak lensing aperture mass. Other studies also find that the stellar mass fraction, when measured sufficiently far away from the brightest cluster galaxy, is approximately constant in groups and clusters (e.g. Bahcall & Kulier, 2014; Budzynski et al., 2014; Zu & Mandelbaum, 2015; Wang et al., 2018). For observables related to the stellar mass of clusters, aperture masses provide mass calibrations with low uncertainty and without any model dependence which is ideal for cluster cosmology.

We would also expect the SZ signal to be sensitive to projection effects since it is independent of redshift, and since its pressure dependence allows it to probe larger scales. However, the steep scaling of the SZ signal with the 3D halo mass due to its scaling with the gas temperature and density, means that low-mass haloes will constitute an approximately constant background that can be corrected for (e.g. Angulo et al., 2012; Le Brun et al., 2015). Hence, the SZ signal is likely less sensitive to projection effects than the cluster stellar mass, but more sensitive than cluster X-ray properties.

A full comparison between the performance of aperture and 3D mass calibrations for different survey observables would require generating mock surveys and mimicking the aperture mass measurement and the 3D mass inference from mock weak lensing observations, which is beyond the scope of this work.

All in all, halo aperture masses provide clear advantages for cluster cosmology. The direct connection between aperture masses measured from simulations and observations make them practically independent from assumptions about the density profile of clusters. Moreover, the relation between the cluster observable of interest and the true cluster aperture mass cleanly separates in a purely observational scaling relation and an intrinsic measurement uncertainty between the observed and the true aperture mass, which can be calibrated using simulations. Next, we turn our attention to the final ingredient for cluster cosmology in Eq. (4.1): the aperture mass function.

## 4.4 Halo aperture mass function

Having introduced the aperture mass and compared it to the 3D halo mass, we now study the aperture mass function. We show how the aperture mass function depends on the aperture mass in Section 4.4.1. Then, we briefly explain how we fit a Gaussian process emulator to capture the cosmology dependence of the

aperture mass function in Section 4.4.2, leaving the details of the implementation to Appendix 4.B and the verification to Appendix 4.C. Finally, we discuss the cosmology sensitivity of the aperture mass function in Section 4.4.3.

#### 4.4.1 Aperture mass function behaviour

We compute the aperture mass function by dividing the number of haloes in mass bins of  $\log_{10} \Delta M$  by the simulated volume and the bin width. The number density,  $n$ , dependent on the cosmological parameters,  $\Omega_i$ , can be defined either as a function of the comoving volume,  $V$ ,

$$n_V(\Delta M, z, \Omega_i) = \frac{dN(\Delta M, z, \Omega_i)}{dV(z, \Omega_i) d\log_{10} \Delta M} \quad (4.4)$$

or as a function of the probed survey volume

$$n_\Omega(\Delta M, z, \Omega_i) = \frac{dN(\Delta M, z, \Omega_i)}{d\Omega(z, \Omega_i) dz d\log_{10} \Delta M}. \quad (4.5)$$

We have introduced the cosmology-dependent differential solid angle,  $d\Omega$ , and the redshift range,  $dz$ . For cosmological simulations,  $n_V$  naturally matches the data since we can divide the mass-binned number counts directly by the comoving simulation volume. The growth of structure from the initial density field fixes the cosmology dependence of the volumetric number density,  $n_V$ . The cosmology dependence of the *observed* halo number density, however, receives an additional geometric contribution since we observe our past lightcone. We obtain the observed number density from the volumetric number density as

$$n_\Omega(\Delta M, z, \Omega_i) = n_V(\Delta M, z, \Omega_i) \frac{dV(z, \Omega_i)}{d\Omega dz}, \quad (4.6)$$

where the geometric conversion depends on the comoving distance and the transverse comoving distance at redshift  $z$  for the assumed cosmology. The conversion scales the amplitude of the volumetric aperture mass in a cosmology and redshift-dependent way. The same geometric factor also applies to the simulated 3D halo mass function.

Since the weak lensing aperture mass receives contributions from structure along the past lightcone weighted by the lensing kernel, technically, the scatter in the aperture mass at fixed halo mass adds a geometry sensitivity to the volumetric aperture mass function. However, as we have shown in Fig. 4.3, for higher-mass haloes this scatter becomes less important compared to the intrinsic scatter due to the differing matter distribution close ( $L \lesssim 30$  cMpc) to the cluster. Hence, neglecting the past lightcone should not significantly change our conclusions.

In what follows, we will initially show results for  $n_V$  as is generally done for the 3D halo mass function in the literature to aid in the interpretation of our results. However, only  $n_\Omega$  includes the full cosmology dependence of both the aperture mass function and the 3D halo mass function. We will use  $n_\Omega$  to investigate the cosmology sensitivity of the aperture mass function in Section 4.4.3.

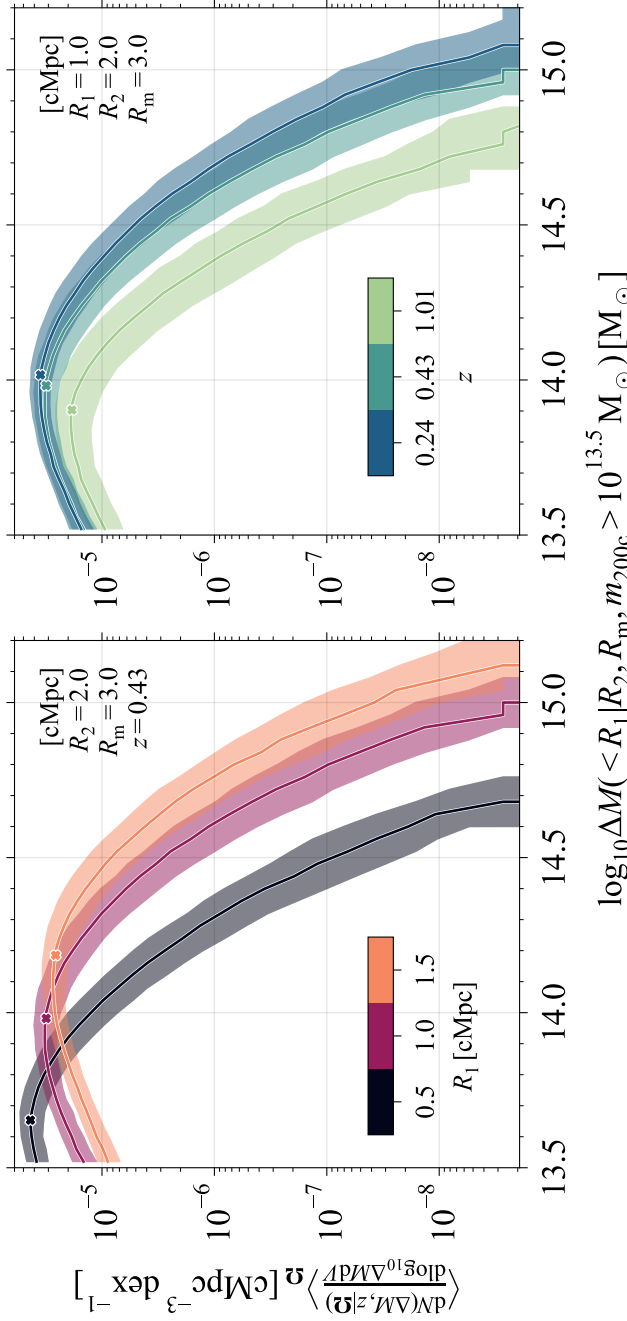


Figure 4.8: *Left panel:* The median aperture mass function, for a fixed comoving volume,  $n_V$ , of all cosmologies in the hypercube for aperture masses measured within different apertures  $R_1$  (thick coloured lines) at  $z = 0.43$  for all haloes with  $m_{200c} > 10^{13.5} M_\odot$ . The shaded regions show the 16th to 84th percentile scatter. The reference annulus for all aperture mass measurements spans the region between  $R_2 = 2$  cMpc and  $R_m = 3$  cMpc. Larger apertures result in higher aperture masses and shift the aperture mass function to the right. The number density decreases for low aperture masses if a significant fraction of the haloes has 3D masses near the selection limit, indicated by the crosses that show the 84th percentile aperture mass for haloes with  $m_{200c,\text{lim}} = 10^{13.5} M_\odot$ . *Right panel:* The redshift evolution of the median aperture mass function with  $R_1 = 1$  cMpc. The number density increases with time as haloes grow more massive. The peak of the aperture mass function shifts to larger values with time due to the increased scatter at the fixed 3D halo mass limit.

In the left-hand panel of Fig. 4.8, we show the median aperture mass function,  $n_V$ , and its 16th to 84th percentile scatter for all cosmologies in the parameter hypercube and aperture masses measured within different apertures. All aperture masses have been computed with the same control annulus between  $R_2 = 2 \text{ cMpc}$  and  $R_m = 3 \text{ cMpc}$ , and only haloes with  $m_{200c} > m_{200c,\text{lim}} = 10^{13.5} M_\odot$  are included within the sample. Since larger apertures will result in higher aperture masses for the same halo, increasing the aperture size shifts the aperture mass function to higher aperture masses. The aperture mass function decreases towards both high and low aperture masses. The former is caused by the rarity of high-mass haloes and the latter by the halo mass selection of the sample and the large scatter in aperture mass at fixed halo mass. When a significant fraction of the haloes at fixed aperture mass has 3D masses near the selection limit, the number density starts decreasing. We show this by highlighting the 84th percentile aperture mass for haloes with 3D masses at the selection limit with a cross. These crosses coincide almost perfectly with the peak in the aperture mass function. The right-hand panel of Fig. 4.8 shows that the aperture mass function increases with redshift as more massive haloes form, just like the traditional halo mass function does. The peak of the aperture mass function shifts towards higher aperture masses with time due to the increased scatter at the fixed 3D halo mass limit (see Fig. 4.6).

In Fig. 4.9, we show how the aperture mass function changes when increasing the 3D mass limit,  $m_{200c,\text{lim}}/M_\odot$ , from  $10^{13.5}$  to  $10^{14.5}$ . The number density for the largest aperture mass haloes is not strongly affected since the scatter in the aperture mass at the mass limit decreases with increasing mass limit. For all mass limits, the cross indicates the 84th percentile aperture mass for haloes with 3D masses at the selection limit. Since the  $\Delta M - m_{200c}$  relation is sublinear, the median aperture mass at  $m_{200c,\text{lim}}$ , and, therefore, also the peak mass increase less strongly than the 3D halo mass when increasing  $m_{200c,\text{lim}}$ . The number density for aperture masses beyond the peak is still affected by the mass limit, albeit less so. Hence, for aperture mass cosmological analyses, it will be important to select clusters using observables that either have small scatter with respect to the aperture mass, or whose scatter is well-understood.

We stress that the haloes in Fig. 4.9 are selected solely based on their 3D halo mass. However, low-mass haloes that scatter to much higher aperture masses than the median relation for their halo mass, are either part of the correlated structure or chance alignments with a massive cluster. In realistic observational scenarios, such haloes would not be part of the cluster sample, as they would blend in with the larger cluster. However, this also requires such haloes to be excluded from the theoretical aperture mass function calculation. The same problem applies to the 3D mass function; end-to-end pipelines are needed to model such effects.

Finally, we investigate the sample variance of the aperture mass function, which we will need to accurately calibrate the emulator. Since large-scale modes can locally and coherently boost or suppress the number counts, the variance of the aperture mass function needs to be estimated by resampling the data over sufficiently large volumes that include the inherent correlation structure. Crocce et al. (2010) and Smith & Marian (2011) have shown that the 3D halo mass function

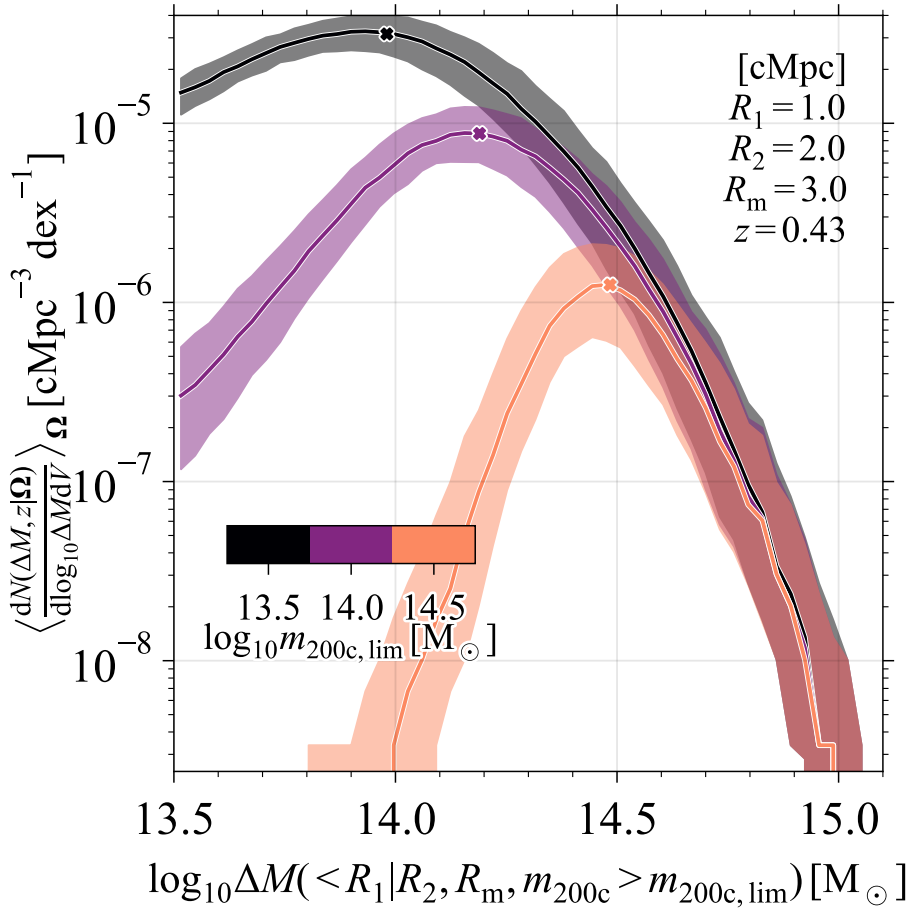


Figure 4.9: The change in the median aperture mass function for a fixed comoving volume,  $n_V$ , for all cosmologies at fixed aperture size when increasing the mass selection limit,  $m_{200c, lim}$ . The thick, coloured lines show the different mass limits,  $m_{200c, lim}$ . The crosses indicate the 84th percentile aperture mass for haloes with  $m_{200c} = m_{200c, lim}$ . The scatter in the aperture mass for haloes at the mass limit sets the peak of the aperture mass function.

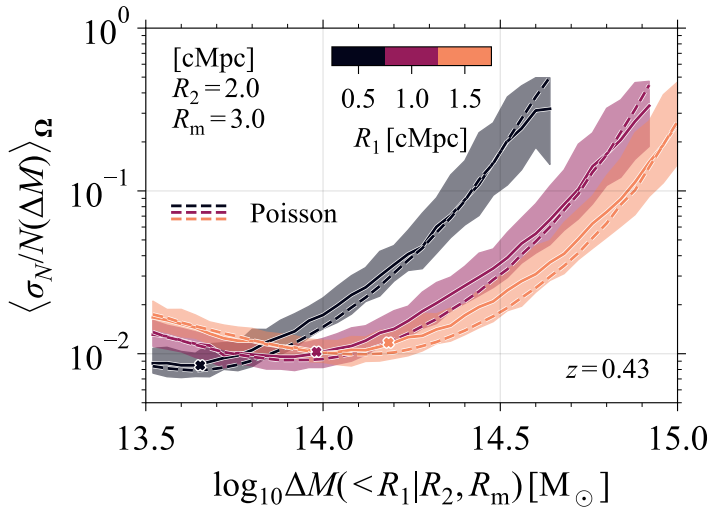


Figure 4.10: The median fractional variance in the aperture mass function for different apertures for all cosmologies at  $z = 0.43$  (solid, coloured lines). All haloes are selected to have  $m_{200c} > 10^{13.5} M_\odot$ . The reference annulus for all aperture mass measurements spans the region between  $R_2 = 2$  cMpc and  $R_m = 3$  cMpc. The shaded regions show the 16th to 84th percentile scatter and the dashed lines show the median shot-noise expectation. The crosses indicate the peak of the aperture mass function. The aperture mass function variance generally exceeds the shot-noise.

4

variance is dominated by Poisson noise at high halo masses, and that a jackknife-type resampling can recover the true variance accurately. For this reason, we use bootstrap resampling to divide the projected mass maps into  $(n, n)$  subregions. We then compute the aperture mass function variance for 10,000 halo samples generated by including  $n^2 = 25$  randomly chosen, possibly repeating, subareas. This way, we can estimate the sample variance of the aperture mass function for cluster samples obtained from an equal simulation volume.

We show the bootstrapped fractional aperture mass variance in Fig. 4.10. We also include the Poisson expectation based on the number of haloes at fixed aperture mass. We find that the sample variance of the aperture mass function exceeds the Poisson expectation by up to a factor of  $\approx 1.5$ , except for the lowest- and highest-aperture mass haloes. We will use the bootstrapped variance estimates for the individual simulations when fitting the aperture mass function emulator in the following Section.

#### 4.4.2 Emulating the aperture mass function

We construct an emulator to infer the general cosmology dependence of the aperture mass function from the available grid of cosmological parameters. Usually,

emulators fit some compressed form of the true underlying data, such as the cosmology dependence of either the parameters of a theoretical fitting function (e.g. McClintock et al., 2019) or the weights of the principal components of either the data or some functional approximation (e.g. Bocquet et al., 2020). However, all these methods assume that those compressed models accurately capture the underlying halo mass function behaviour for all masses. While this assumption can be checked as long as haloes are abundant, it might not hold in the exponentially declining tail which contains important cosmological information, potentially resulting in confident but inaccurate predictions.

We therefore fit a Gaussian process *directly* to the simulated data at each redshift independently, only assuming Gaussian correlations in the latent function and a discrete likelihood for the *observed* number counts. Previously, fitting a Gaussian process directly to large datasets with non-Gaussian likelihoods was not feasible: there was no well-understood and unified way to both account for general, non-Gaussian likelihoods, and deal with the computationally intensive inversion of the covariance matrix in the model optimization. However, since the work of Titsias (2009) and Hensman et al. (2014), this is no longer an issue. We gain a subtle but important advantage by modelling the number counts directly with a Gaussian process: the high-mass tail of cosmological models with no observed clusters can be fit consistently with the correct likelihood and without assuming any functional form for the aperture mass function.

We provide a detailed description of our emulator implementation and the performance in Appendices 4.B and 4.C, respectively, but detail the main insights here. Briefly, we will fit the normalized aperture mass function

$$f(\mathbf{x}_i = (\Delta M, \boldsymbol{\Omega}_i)^T) = \log n(\Delta M, \boldsymbol{\Omega}_i) - \log \langle n(\Delta M, \boldsymbol{\Omega}_i) \rangle_{\boldsymbol{\Omega}}, \quad (4.7)$$

to reduce the dynamic range and the impact of the peak in the aperture mass function on the emulator calibration. We have checked that training the emulator on  $n_V$  and  $n_{\Omega}$ , defined in Eqs. (4.4) and (4.5), respectively, gives consistent performance. Then, we assume a Gaussian process prior for the mean and the variance of  $f$

$$\mathbb{E}[f(\mathbf{x}_i)] = \mu \quad (4.8)$$

$$\text{Var}[f(\mathbf{x}_i), f(\mathbf{x}_j)] = k(\mathbf{x}_i, \mathbf{x}_j), \quad (4.9)$$

where  $k(\mathbf{x}_i, \mathbf{x}_j)$  is the covariance function between inputs  $\mathbf{x}_i$  and  $\mathbf{x}_j$ . We will be using the radial basis function (or squared exponential) kernel for  $k$ :

$$k(\mathbf{x}, \mathbf{x}') = \sigma^2 \prod_{i=0}^d \exp \left( -\frac{((\mathbf{x})_i - (\mathbf{x}')_i)^2}{2\ell_i^2} \right), \quad (4.10)$$

where  $i$  runs over the  $d = 9$  dimensions of  $\mathbf{x}$  and each dimension has its own covariance lengthscale  $\ell_i$ , resulting in hyperparameters  $\theta = (\mu, \sigma^2, \boldsymbol{\ell})$ . The hyperparameters,  $\theta$ , can be optimized to accurately capture the cosmology dependence

of the aperture mass function, assuming the likelihood of the simulated number counts,  $(\mathbf{x}_i, N_i)$ , given the model,  $f(\mathbf{x}_i)$ .

We leave the details of optimizing this Gaussian process to Appendix 4.B, but the scalable, variational inference method developed by Titsias (2009) and Hensman et al. (2014) allows us to fit directly to the large, simulated dataset, assuming a discrete likelihood that naturally matches the simulated number counts, meaning that we do not need to assume any functional form for the aperture mass function.

We find that the Gaussian process emulator is able to predict most of the simulated aperture mass functions to within  $\pm 2$  per cent in the high-abundance regime and to within the shot-noise for high-aperture masses (see Fig. 4.15). The emulator also generalizes well in a leave-one-out-test as it is generally able to predict most simulations within  $\pm 5$  per cent when not including them in the emulator calibration (see Fig. 4.16).

At this point, we are satisfied with the emulator performance in capturing the underlying cosmology dependence of the aperture mass function. However, we want to reiterate that our goal has not been to calibrate the emulator to the level of accuracy required for future surveys. Such an emulator needs to be calibrated specifically to the survey specifications such as the chosen angular aperture size, the probed redshift range, the selection function of the observable, and needs to compute the aperture masses from the full past lightcone. We require the emulator only to be able to investigate how varying individual cosmological parameters affects the aperture mass function.

## 4

### 4.4.3 Cosmology dependence of the aperture mass function

We can use the calibrated emulator to investigate the cosmological sensitivity of the aperture mass function. Previously, Marian et al. (2009, 2010) showed that the aperture mass function for a filter that optimizes the cluster SNR, closely follows the cosmology dependence of the 3D mass function, suggesting a similar cosmology sensitivity. However, their chosen filter required assuming a typical density profile for clusters, which we have been careful to avoid.

Fig. 4.11 shows the sensitivity of the volumetric aperture mass function to changes in individual cosmological parameters (different panels) and the aperture (different line thickness) at fixed redshift. We reiterate that the full cosmology dependence of the *observed* aperture mass function also depends on the geometry through the volume of the past lightcone, as Eq. (4.6) shows. We adopt a fiducial Planck Collaboration et al. (2020) cosmology with  $\Omega \equiv \{\Omega_m, \Omega_b, \Omega_\nu, \sigma_8, h, n_s, w_0, w_a\} = \{0.315, 0.049, 0.0014, 0.811, 0.674, 0.965, -1, 0\}$ , with  $\Omega_\nu$  corresponding to  $M_\nu = 0.06$  eV, and separately vary each of the cosmological parameters by  $\pm 1$  and 5 per cent (different colours). For  $w_a$ , we assume fixed values  $\pm 0.01$  and  $\pm 0.05$ , since the fiducial value is 0. In agreement with the 3D halo mass function, to which we explicitly compare in Fig. 4.13, the shape of the aperture mass function at fixed redshift is most sensitive to changes in  $\sigma_8$  and  $\Omega_m$ , with a  $\pm 1$  per cent change in  $\sigma_8$  ( $\Omega_m$ ) resulting in  $> 10$  per cent (up to 5 per cent) changes in the aperture mass function. Besides  $\Omega_m$  and  $\sigma_8$ , the aperture

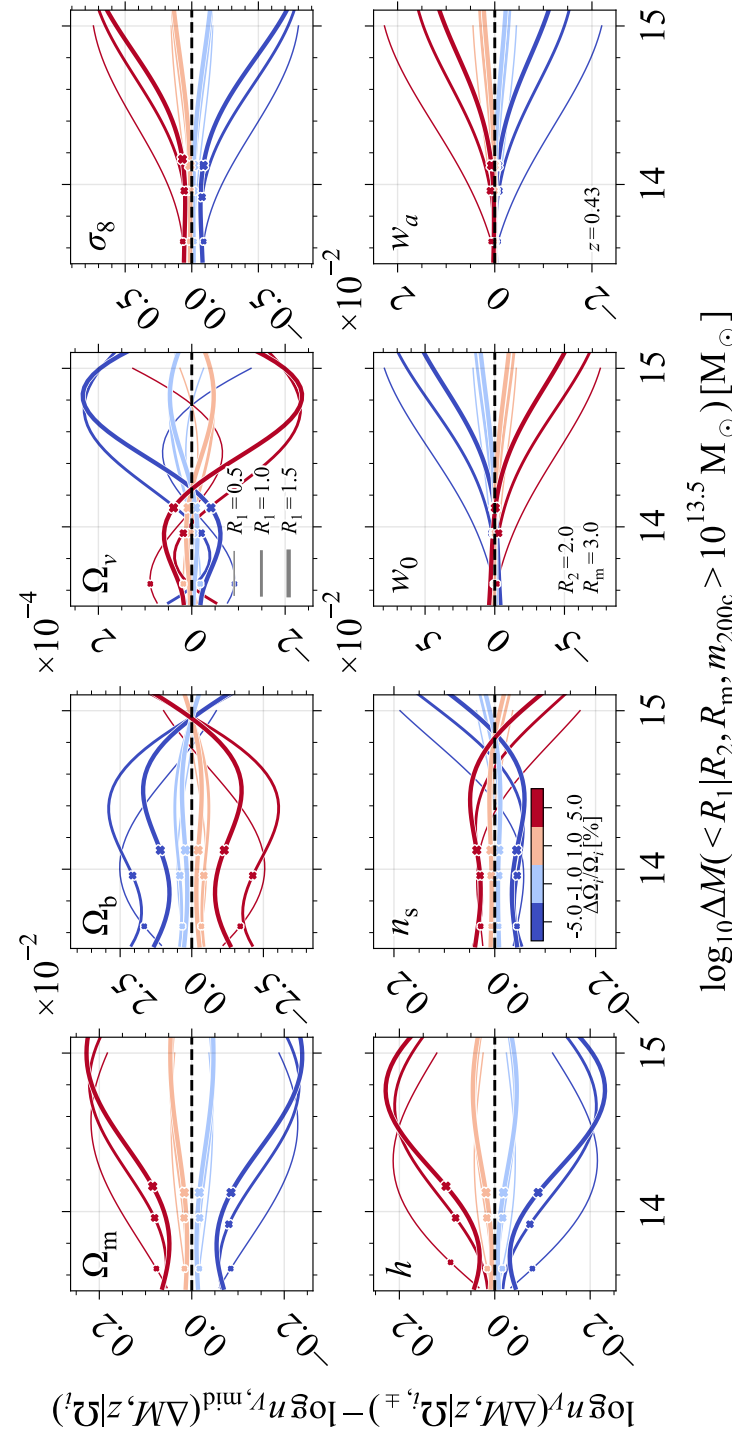


Figure 4.11: The sensitivity of the aperture mass function for a fixed comoving volume,  $n_V$ , to changing individual cosmological parameter values by  $\pm 1.5$  per cent at  $z = 0.43$ . The cosmological parameter being varied is indicated in the top-left corner of each panel (note the different  $y$ -axis scaling for the different parameters). We assume  $w_a = \pm 0.01, \pm 0.05$  since the fiducial value is 0. Coloured lines indicate the fractional change in the individual cosmological parameters with respect to the fiducial Planck Collaboration et al. (2020) cosmology, with the line thickness varying from thin to thick for  $R_1 = 0.5, 1.0, 1.5$  cMpc. All aperture masses were measured with  $(R_2, R_m) = (2, 3)$  cMpc and all haloes have  $m_{200c} > 10^{13.5} M_\odot$ . The peak of the aperture mass function is indicated with a cross. Increasing the aperture size mainly shifts the aperture mass function to higher masses. The amplitude also changes noticeably for different aperture sizes when varying  $\Omega_b$  and  $\Omega_\nu$ . The aperture mass function is most sensitive to changes in  $\sigma_8$ ,  $\Omega_m$ , and  $h$ , with additional sensitivities to the scalar spectral index of the initial power spectrum,  $n_s$ , and the dark energy equation-of-state parameters  $w_0$  and  $w_a$ .

mass function is also sensitive to both the dimensionless Hubble parameter,  $h$ , and the scalar spectral index of the linear power spectrum,  $n_s$ . The equation-of-state parameters,  $w_0$  and  $w_a$ , mainly affect the abundance of high-aperture mass haloes. Increasing the aperture size shifts the aperture mass function to larger aperture masses. However, apart from this approximate shift for different aperture sizes, the amplitude of the aperture mass function also changes noticeably for  $\Omega_b$  and  $\Omega_\nu$ .

In Fig. 4.12, we show the cosmology sensitivity of the aperture mass function for masses measured within  $R_1 = 1$  cMpc at different redshifts. At all redshifts, the aperture mass function is most sensitive to changes in  $\sigma_8$ ,  $\Omega_m$ , and  $h$ . For most cosmological parameter changes, the abundance changes more strongly at higher redshifts. Noticeably, the dark energy equation-of-state parameters affect the halo abundance more significantly at higher redshifts. The peak of the aperture mass function, which is indicated with a cross, shifts to higher aperture masses with decreasing redshift.

The dominant cosmology dependence of the aperture mass function can be understood from the 3D halo mass function, since

$$n(\Delta M, z|\boldsymbol{\Omega}) = \int_0^\infty dm_{200c} n(m_{200c}, z|\boldsymbol{\Omega}) P(\Delta M, z|m_{200c}, \boldsymbol{\Omega}). \quad (4.11)$$

The large scatter in aperture mass at fixed 3D halo mass does cause differences in the detailed mass dependence. In Fig. 4.13, we compare the cosmology sensitivity of the 3D halo mass function (dash-dotted lines) and aperture mass function (solid lines) for the median aperture mass at  $m_{200c}$  for all cosmologies in the hypercube,  $\langle \Delta M | m_{200c} \rangle_{\boldsymbol{\Omega}}$ . The individual cosmological parameters vary by  $\pm 5$  per cent around the Planck Collaboration et al. (2020) best-fit parameters (coloured lines in the different panels). For the 3D halo mass function, the peak height of haloes determines their abundance, with more significant peaks being less abundant. Increasing  $\sigma_8$  while fixing the remaining cosmological parameters boosts the average variance on all scales equally, which decreases the peak height at all halo masses and results in an increased abundance, as can be seen in the top-right panel of Fig. 4.13. In the exponentially declining tail, the constant decrease in the peak height increases the abundance more dramatically. The aperture mass function follows these trends.

When changing the other cosmological parameters, it is important to remember that we fix  $\sigma_8$ , implying that the initial normalization of the matter power spectrum,  $A_s$ , does change. Fixing  $\sigma_8$  instead of  $A_s$  reduces the impact of changing the other cosmological parameters on the mass function. Increasing  $\Omega_m$  in a flat universe will result in deeper dark matter potential wells, a faster growth of structure, and a delayed onset of dark energy domination. The peak height decreases for all haloes, resulting in higher abundances. The top-left panel of Fig. 4.13 shows that the abundance of low-aperture mass haloes changes less than the 3D halo mass function for low halo masses due to the increasing incompleteness at fixed, low aperture mass (see Fig. 4.9). At high aperture masses the large scatter in aperture mass at fixed  $m_{200c}$  results in a larger sensitivity of the aperture

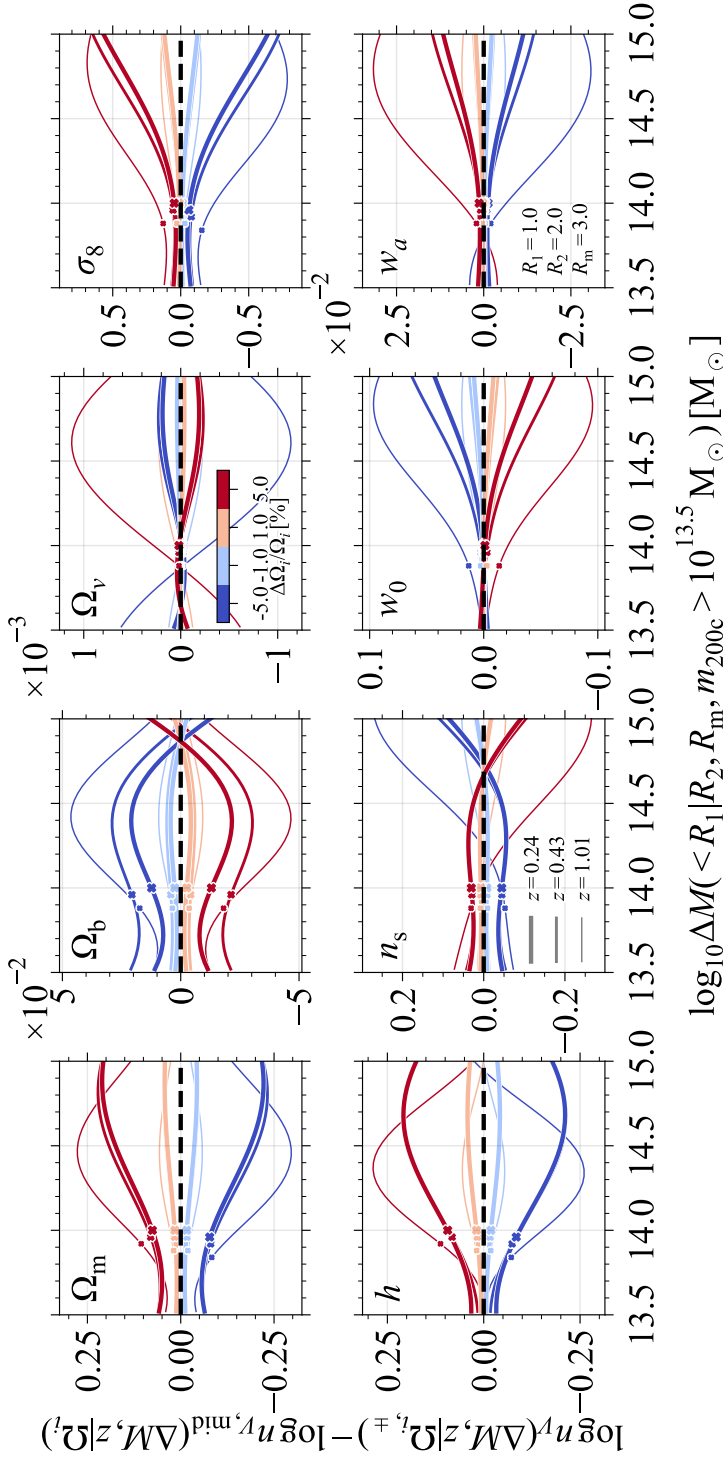


Figure 4.12: The sensitivity of the aperture mass function for a fixed comoving volume,  $n_V$ , to changing individual cosmological parameter values by  $\pm 1.5$  per cent for  $R_1 = 1$  cMpc and different redshifts. We assume  $w_a = \pm 0.01, \pm 0.05$  since the fiducial value is 0. The cosmological parameter being varied is indicated in the top-left corner of each panel. Coloured lines indicate the fractional change in the individual cosmological parameters with respect to the fiducial Planck Collaboration et al. (2020) cosmology, with the line thickness varying from thick to thin for the redshifts  $z = 0.24, 0.43, 1.01$ . All aperture masses were measured with  $(R_1, R_2, R_m) = (1, 2, 3)$  cMpc, and all haloes have  $m_{200c} > 10^{13.5} M_\odot$ . The peak of the aperture mass functions is indicated with a cross. The peak of the mass function shifts to higher masses for lower redshifts. The aperture mass function is most sensitive to changes in  $\sigma_8$ ,  $\Omega_m$ , and  $h$ . The relative impact of changing the cosmological parameters on the abundance increases with redshift.

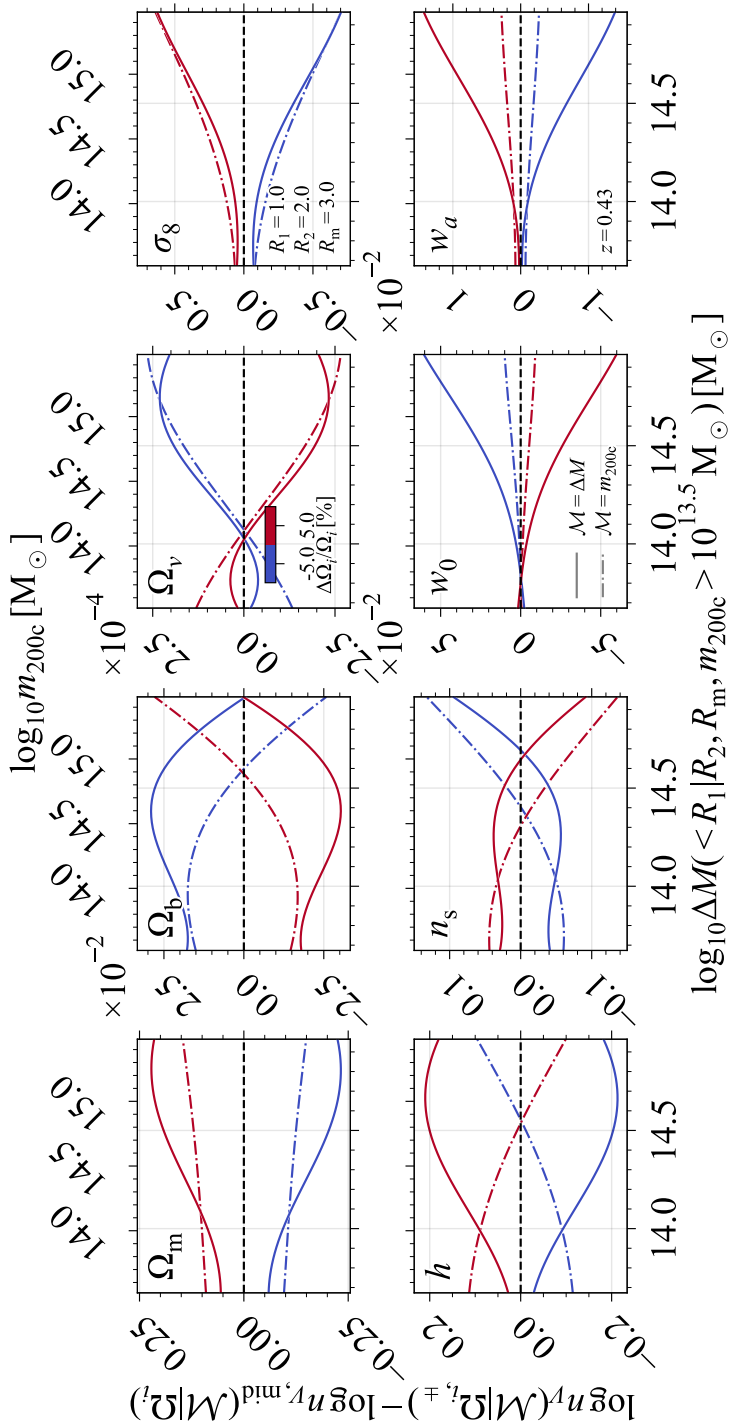


Figure 4.13: Comparison between the cosmology sensitivity of the 3D halo mass function (dash-dotted lines) and the aperture mass function (solid lines), for a fixed comoving volume, to changing individual cosmological parameter values by  $\pm 5$  per cent at  $z = 0.43$ . We assume  $w_a = \pm 0.05$  since the fiducial value is 0. The aperture mass function is plotted for the median aperture mass at  $m_{200c}$  for all the simulations in the hypercube, and for apertures  $(R_1, R_2, R_m) = (1, 2, 3)$  cMpc. All haloes have  $m_{200c} > 10^{13.5} M_\odot$ . The cosmological parameters are indicated in the top-left corner of each panel. Coloured lines indicate the fractional change in the individual cosmological parameters with respect to the fiducial Planck Collaboration et al. (2020) cosmology. Both the 3D mass and the aperture mass function show similar sensitivity to changes in the  $\sigma_8$ ,  $n_s$ ,  $w_0$  and  $\Omega_\nu$ . The aperture mass function is more sensitive to changes in  $\Omega_m$ ,  $h$ , the dark energy equation-of-state parameters,  $w_0$  and  $w_a$ , and  $\Omega_b$ .

mass function compared to the 3D halo mass function due to the contribution of abundant low-mass haloes.

Increasing  $h$  at fixed  $\Omega_m$  increases the density which results in faster structure formation and makes haloes at fixed  $m_{200c}$  more compact, decreasing their peak height and increasing their abundance. The aperture mass function is significantly more sensitive to changes in  $h$  than the 3D halo mass function. Increasing the scalar spectral index,  $n_s$ , at fixed  $\sigma_8$  shifts the power from large to small scales, resulting in more low-mass and fewer high-mass haloes for both the 3D and the aperture mass function. Finally, increasing the magnitude of the equation-of-state parameter of dark energy,  $w_0$ , dampens the growth of the most massive haloes, reducing their abundance. Again, the aperture mass function is more sensitive to these changes than the 3D halo mass function.

Finally, in Fig. 4.14, we compare the volumetric mass functions, defined in Eq. (4.4) (thin lines), to the observed mass functions including the cosmology-dependent volume of the past lightcone, defined in Eq. (4.5) (thick lines), for both the 3D halo mass function (dash-dotted lines) and the aperture mass function (solid lines). Changing the background evolution of the Universe modifies the number of observed haloes per fixed solid angle,  $d\Omega$ , and redshift interval,  $dz$ , due to the change in the probed comoving volume. The background evolution does not depend on  $\sigma_8$ ,  $n_s$ , and  $\Omega_b$  (since  $\Omega_m$  is fixed).

The background evolution is most sensitive to changes in the Hubble parameter. Increasing (decreasing)  $h$  reduces (increases) the distance to redshift  $z$ . As a result, a fixed survey area at redshift  $z$  will probe a smaller (larger) comoving volume. Hence, we would observe fewer (more) haloes for a fixed volumetric number density. The bottom-left panel of Fig. 4.14 shows that the decrease in the probed volume is larger than the increase in the volumetric number density due to the increased matter density. Changing  $h$  results in the largest difference between the observed and the volumetric mass functions, making the 3D halo mass function more sensitive to changes in  $h$ , and the aperture mass function less sensitive.

Increasing the matter density,  $\Omega_m$ , similarly reduces the probed volume for a fixed survey area at fixed redshift. This suppresses the observed number density,  $n_\Omega$ , compared to the volumetric number density,  $n_V$ , for both the 3D halo mass function and the aperture mass function. The aperture mass function is still more sensitive to changes in  $\Omega_m$  than the 3D halo mass function. The comoving volume for a fixed area on the sky increases (decreases) significantly when increasing (decreasing) the magnitude of  $w_0$ , resulting in more (fewer) observed haloes. This geometric effect is stronger than the decrease (increase) in the volumetric number density due to the less (more) efficient structure formation. Increasing (decreasing)  $w_a$  decreases (increases) the magnitude of  $w(z)$  for  $z > 0$ , which in turn lowers (raises) the observed number density compared to the volumetric number density. The aperture mass function becomes less sensitive to changes in  $w_0$  and  $w_a$ . However, compared to the 3D halo mass function, the total sensitivity to changes in  $w_a$  remains higher and the sensitivity to  $w_0$  becomes similar.

Providing a detailed comparison between the performance of aperture masses and 3D halo masses in a cluster cosmology analysis is more complicated than

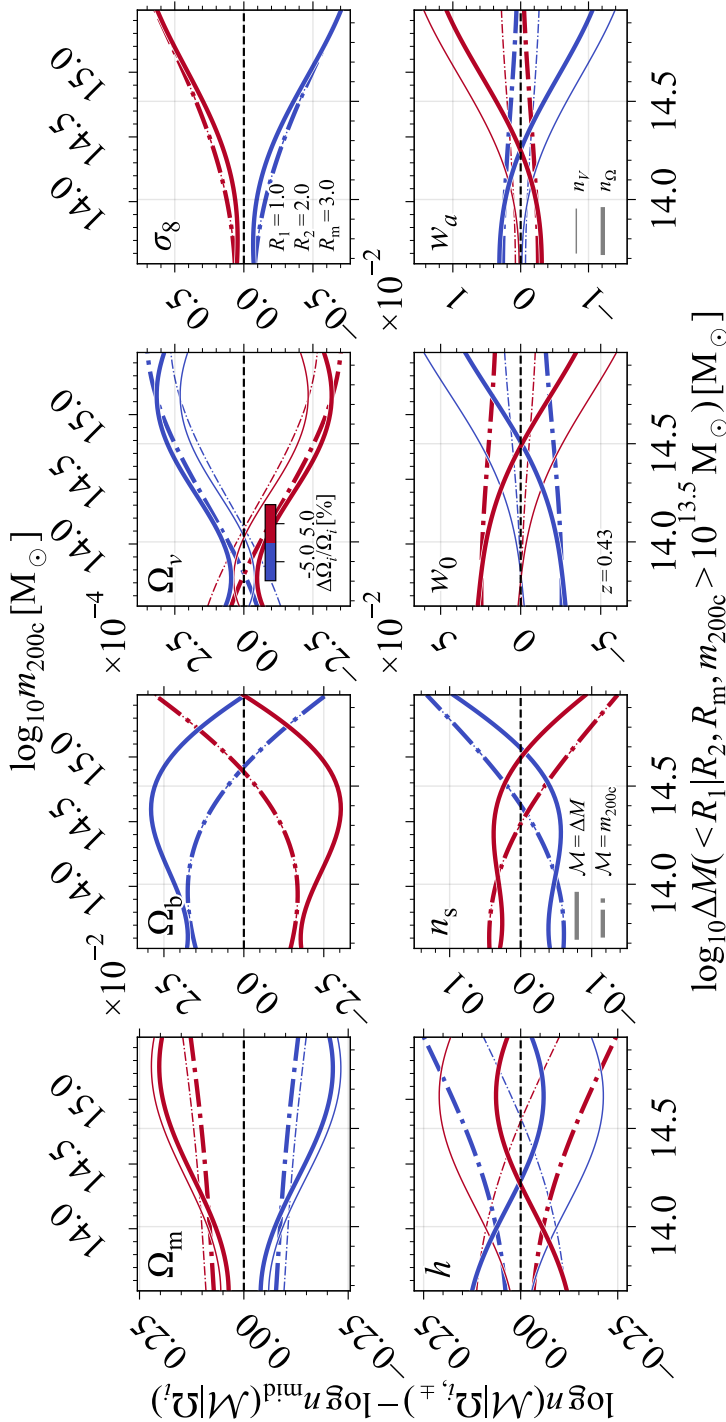


Figure 4.14: Comparison between the cosmology sensitivity of the 3D halo mass function (dash-dotted lines) and the aperture mass function (solid lines) with ( $n_\Omega$ , thick lines) and without ( $n_\nu$ , thin lines) including the cosmology dependence of the survey solid angle and redshift interval at  $z = 0.43$ . The cosmological parameter being varied by  $\pm 5$  percent (coloured lines) with respect to the fiducial Planck Collaboration et al. (2020) cosmology is indicated in the top-left corner of each panel. We assume  $w_a = \pm 0.05$  since the fiducial value is 0. The aperture mass function is plotted for the median aperture mass at  $m_{200c}$  for all the simulations in the hypercube, and for apertures  $(R_1, R_2, R_m) = (1, 2, 3)$  cMpc. All haloes have  $m_{200c} > 10^{13.5} M_\odot$ . The probed comoving volume for a fixed observed area is mainly sensitive to  $h$ ,  $\Omega_m$ ,  $w_0$  and  $w_a$ . Compared to the 3D halo mass function, the aperture mass function is more sensitive to changes in  $\Omega_m$  and  $w_a$ , similarly sensitive to  $\sigma_8$  and  $w_0$ , and less sensitive to  $h$ .

investigating the percentage differences in the mass functions given a difference in the cosmological parameters. Eq. (4.1) shows that the number counts depend on the integral over the mass function taking into account the uncertainty in the mass–observable relation. Even though we have shown that the intrinsic measurement uncertainty in aperture mass measurements is much lower than that in 3D halo mass inference, the total uncertainty in the mass–observable relation still depends on the scatter between the survey selection observable and the measured aperture or 3D mass. For surveys that do not select clusters based on their weak lensing shear signal, the scatter in the observable at fixed aperture mass can still result in a significant total uncertainty in the aperture mass–observable relation. Hence, a comparison between 3D and aperture mass calibrations in a full cosmological analysis also needs to take into account the survey observable.

In conclusion, the sensitivity of the aperture mass function to small changes in the cosmological parameters opens the possibility of calibrating cluster masses with weak lensing aperture masses, bypassing the modelling uncertainty introduced when deprojecting the observations.

## 4.5 Discussion

4

We have provided arguments for calibrating cluster masses with weak lensing aperture masses. As long as we do not have predictions for the halo abundance directly as a function of the survey observable, such as the galaxy overdensity, the X-ray luminosity, or the SZ signal, cluster cosmology needs to follow a two step process. Assuming that the selection function has been accounted for, the mass–observable relation needs to be calibrated, and the cosmology dependence of the mass function needs to be understood. Eq. (4.1) shows that the mass calibration requires both the calibration between the observable and the mass inferred from observations, and the calibration between the inferred mass and the theoretical mass used in the mass function.

To more closely match weak lensing observations, it makes sense to calibrate cluster masses with the projected aperture mass, which can also be measured in simulations. The mass calibration then separates cleanly into a purely observational relation between the measured aperture mass and the observable, and a calibration between the theoretical and the measured aperture mass. This clean separation does not hold for 3D cluster masses, which can only be inferred by deprojecting the observations under the assumption of a density profile. Any mismatch between the assumed and the true cluster density profile biases the inferred 3D masses. The large variation in the matter distribution along the lines-of-sight to different clusters adds further uncertainty.

We showed that aperture masses correlate strongly with the 3D mass, albeit with large scatter due to the matter along the line-of-sight. We found that the aperture masses can be measured much more precisely than 3D masses, since the precision is only limited by the shape noise of the background galaxies. Next, we calibrated an emulator to reproduce the cosmology dependence of the aperture

mass function, finding that it is also highly sensitive to variations in the cosmological parameters. Now we will discuss some of the difficulties that arise in cluster cosmology, and how they affect the aperture mass specifically. We will also position our contribution within the wider literature.

#### 4.5.1 Impact of the selection function

One vital ingredient of a cluster cosmology analysis that we did not discuss in this paper is the selection function of the cluster sample. The completeness, i.e. the fraction of all clusters that is detected, and the purity, i.e. the fraction of detections that are real clusters, of the cluster sample should be as high as possible (e.g. Allen et al., 2011; Aguena & Lima, 2018). We have studied the aperture mass function in the idealized setting of perfect purity since we have centred directly on the known clusters in the simulations. Our halo sample becomes increasingly incomplete for aperture mass bins that contain a significant fraction of haloes with 3D masses near our selection limit, as can be seen from Fig. 4.9. Future aperture mass function emulators should thus ensure that they can reliably measure aperture masses for haloes with masses significantly below the expected detection limit of the survey, which we were unable to do due to the downsampling inherent to the Mira–Titan particle catalogues (although this is not a problem in principle for simulations).

Since haloes with masses below the mean expected mass at the observable selection limit can scatter above the signal threshold, the completeness of the cluster sample near the selection limit depends on the scatter of the mass–observable relation (e.g. Mantz, 2019). The main benefit of aperture masses is the ease with which they can be measured both in simulations and in observations, which significantly decreases the intrinsic measurement uncertainty in the mass calibration,  $P(\mathcal{M}_{\text{obs}}|\mathcal{M})$ , compared to 3D masses, as we showed in Section 4.3.3. However, this gain can be lost if the observable used to select clusters has a significantly larger scatter at fixed aperture mass compared to its scatter at fixed 3D mass. Hence, aperture masses could greatly increase the performance of cluster surveys based on observables that correlate with the aperture mass with small uncertainty. This will be the case for observables that are more sensitive to projection effects, such as the SZ signal (e.g. Hallman et al., 2007), galaxy overdensities (e.g. van Haarlem et al., 1997; Erickson et al., 2011), and, naturally, the shear signal.

The purity of the halo sample will depend sensitively on the cluster detection method, with shear-selected samples only reaching a maximum purity of  $\approx 85$  per cent since chance line-of-sight alignments can generate a significant signal due to the broadness of the lensing kernel (e.g. Hennawi & Spergel, 2005). The purity of other detection methods that are also susceptible to such projection effects, such as the SZ signal or the galaxy overdensity, will need to be modelled in simulations. Baryonic observables that predominantly trace the inner cluster density profile, such as the X-ray luminosity, on the other hand, should reach higher purity (e.g. Voit et al., 2001). However, samples selected from these observables are necessarily more sensitive to the halo density profile, introducing possible detection biases near the selection limit (e.g. Chon & Böhringer, 2017).

We highlight one final important point about the synergy between observed and simulated aperture mass measurements. Since the detection bias for observables such as the SZ signal and the galaxy overdensity is in large part due to projection effects (e.g. Shirasaki et al., 2016; Zhang & Annis, 2022), this bias is naturally included in aperture masses measured in simulations. Hence, emulators calibrated on a cluster sample generated by mimicking the survey selection in the simulations will naturally include the survey detection bias while providing aperture mass measurements that are directly comparable to those measured observationally.

#### 4.5.2 Impact of systematic uncertainties

In a realistic cosmological analysis, different observational systematic effects need to be taken into account. Any weak lensing mass measurement will be sensitive to the systematic errors in the shape measurements, the redshift distribution of the sources, contamination of the lensing signal due to uncertainty in the photometric redshift determination of cluster galaxies, and miscentring of the cluster (e.g. Von der Linden et al., 2014; Hoekstra et al., 2015).

The main advantage of aperture masses over 3D masses is that no density profile needs to be assumed in the analysis, eliminating the impact of this modelling uncertainty. The aperture mass within  $R_1$  is actually measured from the lensing signal of galaxies *outside*  $R_1$ , significantly reducing the impact of sources of systematic error near the cluster centre, such as miscentring and contamination (e.g. Mandelbaum et al., 2010). The optimal choice of  $R_1$  balances the reduced contamination of the lensing signal by cluster galaxies when increasing  $R_1$  against the increase in the statistical uncertainty due to the reduced number of background galaxies. Since the bulk of the haloes have miscentring radii  $< 0.2R_{500c}$  (e.g. Saro et al., 2015; Bleem et al., 2020), apertures can be chosen large enough such that the mass within the aperture should only be slightly affected, while limiting the increased statistical uncertainty.

Another advantage stems from the fact that aperture masses can always be computed unambiguously, even for triaxial and merging systems. As long as the choice of aperture in the mass function and the observations is consistent, the mass measurement should yield similar results. Moreover, since emulators can be calibrated for different aperture sizes, the consistency of the inferred cosmology for an analysis using different apertures can pinpoint possible biases in the cosmological analysis.

A limitation of our preliminary study is the fact that we did not construct convergence maps from the full past lightcone. The lensing efficiency of matter structures at redshift  $z_l$  for source galaxies at a fixed redshift  $z_s$ ,  $\epsilon(z_l, z_s) = D_l D_{ls} / D_s$ , is very broad. This means that matter over a significant range of redshifts can contribute to the lensing signal of a given background galaxy. A full line-of-sight in simulation M000 with  $L = 2100$  cMpc at  $z = 0.5$  corresponds to a redshift range  $z \approx [0.2, 0.85]$ . Hence, projecting the mass along the simulation volume at fixed  $z$  does not take into account the time evolution of the included structures or the change in the angular diameter distance across the length of the box. As

such, aperture mass functions should really be calibrated on simulation lightcone outputs, not on single snapshots. This makes the analysis more complex since the resulting lensing maps need to be reconstructed for different source redshifts,  $z_s$ .

Finally, since we have used gravity-only simulations, we have not included the impact of baryonic physics on the aperture mass function. For 3D halo mass functions, it is well established that the mass of haloes with  $m_{200m,dmo} \lesssim 10^{14.5} M_\odot$  decreases significantly due to galaxy formation physics processes (e.g. Velliscig et al., 2014). We expect baryonic physics to also impact the cluster aperture mass measurements, albeit less significantly due to the projected nature of the measurement (e.g. Debackere et al., 2021). We study the impact of baryonic physics on the aperture mass measurements in a companion paper Debackere et al. (2022).

#### 4.5.3 Comparison to previous work

The abundance of clusters is a powerful probe of the cosmological evolution of the Universe, so an active effort is underway to minimize the impact of mass calibration uncertainties. For example, Grandis et al. (2021) directly calibrate the mass–observable relation,  $P(\mathcal{O}|\mathcal{M})$ , using simulations. They generate lensing profiles from hydrodynamical simulations which they fit with NFW density profiles with a fixed concentration and assuming a miscentring distribution. They then calibrate the resulting relation between the best-fit NFW mass and the true mass of the matched cluster in DMO simulations. This method then converts a weak lensing-inferred 3D halo mass into the 3D halo mass of the matching DMO halo, allowing the use of 3D halo mass function emulators calibrated on DMO simulations. This method is still explicitly limited by the scatter between the inferred and the true 3D halo mass due to the assumed density profile.

Cromer et al. (2021) improve the accuracy of weak lensing-inferred 3D halo masses by fitting the lensing shear with an emulated cluster density profile that includes a phenomenological contribution due to baryons. Their model results in more accurate cluster mass estimates, but, again, relies on the ultimately inaccurate assumption that the complex cluster density profile can be modelled accurately with simplified, spherically symmetric profiles.

Marian et al. (2009, 2010) carry out analyses that are the most similar to ours. They generate lensing maps for different slabs in DMO simulations to which they apply a hierarchical peak finder that extracts the aperture mass within a filter designed to optimally detect the cluster signal. They show that the resulting peak abundance function has a similar cosmological sensitivity as the 3D mass function. Similarly to us, they find that the peak aperture masses show a large scatter at fixed halo mass. However, at the time of their work, large suites of cosmological simulations and emulators were not yet available. Hence, they resorted to constructing an analytic framework to extract cosmological information from weak lensing peak counts.

Another option is to neglect the cluster selection entirely and use the distribution of shear peaks as a function of their signal-to-noise ratio to constrain the

cosmology (see e.g. Wang et al., 2009; Dietrich & Hartlap, 2010; Kratochvil et al., 2010). However, since the evolution of clusters with time contains a wealth of cosmological information, stronger cosmological constraints can be obtained by including redshift information for the observed peaks, as suggested by Hennawi & Spergel (2005). The main difficulty with these shear-selected analyses is that a significant fraction of the high significance peaks arises from chance line-of-sight alignments due the broadness of the lensing kernel (e.g. Hennawi & Spergel, 2005; Yang et al., 2011). In recent studies, Hamana et al. (2015), Shan et al. (2018) and Martinet et al. (2018) have used peaks identified from weak lensing observations to constrain the matter density and clustering of the Universe.

We locate our work in between peak abundance studies and cluster analyses based on 3D cluster masses: our method corresponds to an idealized survey that selects clusters based on a secondary observable that perfectly correlates with the 3D halo mass, while the cluster masses are determined through aperture masses which would in practice be derived from weak lensing observations. Hence, our work is very similar to a standard cluster cosmology analysis, as worked out in detail by Mantz et al. (2010a,b), but now using the aperture mass to calibrate the cluster masses. In such an analysis, one assumes a functional form for the mass–observable relation, which gets calibrated simultaneously with the cosmology-dependent aperture mass function by forward modelling the observed cluster abundance as a function of the observable signal, taking into account the selection function of the observable for a given survey. Importantly, any cosmology dependence in the mass–observable relation needs to be taken into account implying that the cosmology dependence of both  $P(\Delta M_{\text{obs}}|\Delta M, \Omega, z)$  and  $P(\mathcal{O}|\Delta M_{\text{obs}}, \Omega, z)$  need to be calibrated from mock observations in realistic cosmological and, preferably, hydrodynamical simulations (e.g. Dietrich et al., 2019).

## 4.6 Conclusions

We have argued that cluster cosmology analyses can decrease their sensitivity to modelling assumptions by using weak lensing-like excess aperture mass measurements to calibrate cluster masses. As long as predictions for the cosmology-dependent abundance of clusters as a function of their observed signal are not available, cluster cosmology necessarily relies on an accurately determined and well-understood mass–observable relation and a theoretical prediction for the cosmology dependence of the mass function. Only suites of large-volume simulations with varying cosmological parameters can predict the mass function at the accuracy required for future surveys. If we are using simulations, however, we might as well predict the aperture mass function instead of (or along with) the 3D halo mass function.

Aperture masses are a natural choice for cluster mass calibrations since they can be measured accurately both in observations and in simulations, with an uncertainty determined solely by the background galaxy shape noise in the weak lensing observations. In contrast, 3D halo masses can only be inferred by de-

projecting observations assuming a density profile. The mismatch between the assumed density profile and the true, triaxial halo density profile, including substructure and correlated matter, and the neglected matter along the line-of-sight, introduce a model-dependent bias and scatter in the inferred mass.

We used the Mira–Titan suite of large-volume, DMO simulations to measure the excess projected mass of clusters within fixed aperture sizes of  $R_1 = 0.5, 1.0, 1.5 \text{ cMpc}$  with a background subtraction calculated in an outer annulus between  $2 < R/\text{cMpc} < 3$ . We studied the behaviour of these aperture masses and the corresponding aperture mass function. We showed that the aperture mass correlates strongly with the 3D halo mass, with aperture masses being larger (smaller) than the halo virial mass when measured within apertures larger (smaller) than the virial radius (Fig. 4.5). The aperture mass exhibits large scatter at fixed halo mass when the halo virial radius is not significantly larger than the aperture due to the contribution of matter outside the halo (Fig. 4.6). Advantageously, the uncertainty in the *measurement* of the aperture mass is between 2 to 3 times smaller than that of the inferred 3D mass (Fig. 4.7). This is because the measurement uncertainty depends only on the background galaxy shape noise in the weak lensing observations, and since line-of-sight structures contribute to the aperture mass signal whereas they introduce noise in the deprojection for 3D masses.

We did not investigate the scatter between the survey observable and the aperture mass since the Mira–Titan suite does not include hydrodynamics to model the complex baryonic processes related to galaxy formation. However, we argued that observables such as the SZ signal, the galaxy overdensity, and the shear should correlate strongly with aperture masses with small uncertainty, since they are also sensitive to line-of-sight matter structures beyond the halo. X-ray luminosities, on the other hand, due to their steep scaling with the 3D halo mass, may show large scatter at fixed aperture mass, similarly to the 3D halo mass. The uncertainty between the observable and the measured aperture mass will ultimately determine the scatter in the mass–observable relation, given the small intrinsic scatter of the measured aperture mass with respect to the true aperture mass. Investigating the uncertainty between the observable and the measured aperture mass in hydrodynamical simulations is a fruitful direction for future research.

We used the Mira–Titan hypercube of DMO simulations to calibrate a Gaussian process emulator to *directly* emulate the cosmology dependence of the aperture mass function given the simulated number counts and their likelihood, i.e. without assuming an underlying, dimensionality-reducing model for the simulation data. This is possible thanks to advances in Gaussian process modelling, allowing for the efficient optimization of large datasets and non-Gaussian likelihoods. We argued that this gives an advantage over usual emulators since the high-mass tail of the emulator will only depend on the simulation data and the assumed likelihood, *not* on the assumed mass dependence for the assumed data model. We showed that the emulator can accurately reproduce most of the simulations to within 2 per cent or within the bootstrapped variance at high-aperture masses (Fig. 4.15).

Isolating the influence of structure formation on the halo abundance, we found that, compared to the 3D halo mass function, the aperture mass function is sim-

ilarly sensitive to changes in  $\sigma_8$  and  $n_s$ , and more sensitive to changes in  $\Omega_m$ ,  $h$ ,  $w_0$  and  $w_a$  (Fig. 4.13). Even  $\pm 1$  per cent changes in  $\Omega_m$ ,  $\sigma_8$ , and  $h$  result in  $> 10$  per cent changes in the expected halo number density at fixed redshift (Fig. 4.11). Including the cosmology dependence of the volume probed by the past lightcone, we found that, compared to the 3D halo mass function, the aperture mass function is more sensitive to changes in  $\Omega_m$  and  $w_a$ , similarly sensitive to changes in  $\sigma_8$  and  $w_0$  and slightly less sensitive to changes in  $h$  (Fig. 4.14). We stress that a detailed comparison between the performance of the aperture mass function compared to the 3D halo mass function also needs to take into account the survey observable. Importantly, since emulators can easily be calibrated for multiple apertures, the consistency of the inferred cosmology for an analysis using different apertures can provide useful insights into possible biases in the cosmological analysis.

In the future, it will be possible to emulate cluster surveys using lightcones output from hydrodynamical simulations, mimicking the observable measurement and selection directly while skipping the mass calibration step (given that one can trust the simulation predictions at the accuracy required for future surveys, or marginalize over the simulation uncertainty). To validate the fidelity of such simulations, aperture masses provide the best choice to test the simulated mass–observable relations. Since no such simulations are currently available, however, we argue that our approach provides a valuable intermediate step. Emulators of the aperture mass function, which is closer to the data than the 3D halo mass function, can already be trained, minimizing the impact of uncertain modelling assumptions on cluster cosmology analyses.

## 4

## Acknowledgements

We would like to thank the referee for a clear report that helped clarify the aim of our work. This work is part of the research programme Athena with project number 184.034.002 and Vici grants 639.043.409 and 639.043.512, which are financed by the Dutch Research Council (NWO). Argonne National Laboratory’s work was supported under the U.S. Department of Energy contract DE-AC02-06CH11357. This research was supported in part by DOE HEP’s Computational HEP program. This research used resources of the Argonne Leadership Computing Facility at the Argonne National Laboratory, which is supported by the Office of Science of the U.S. Department of Energy under Contract No. DE-AC02-06CH11357. This work also used resources of the Oak Ridge Leadership Computing Facility, which is a DOE Office of Science User Facility supported under Contract DE-AC05-00OR22725.

## Data availability

The data used in this paper is available upon request to the first author.

## 4.A Weak lensing measurements of the aperture mass

In this appendix we show how aperture mass measurements from weak lensing observations relate directly to aperture masses measured from simulations. Over-densities in the mass distribution modify the light propagation from background galaxies depending on the projected distance from the overdensity, distorting the galaxy shapes. By measuring the average shape distortion of a large sample of background galaxies within some annular region, we can derive the total mass contained within that annulus without making any assumptions about the mass distribution.

In general, weak lensing-derived aperture masses are filtered measurements of the surface mass density centred on a position  $\boldsymbol{\theta}_0$ , with a filter function  $U(\boldsymbol{\theta} - \boldsymbol{\theta}_0)$ . We follow the notation of Bartelmann & Schneider (2001) and write

$$M_{\text{ap}}(\boldsymbol{\theta}_0) = \int d^2\boldsymbol{\theta} U(\boldsymbol{\theta} - \boldsymbol{\theta}_0) \kappa(\boldsymbol{\theta}). \quad (4.12)$$

We have introduced the convergence

$$\kappa(\boldsymbol{\theta}) = \frac{\Sigma(\boldsymbol{\theta})}{\Sigma_c}, \quad (4.13)$$

where the critical surface mass density  $\Sigma_c$ , which sets the magnitude of the lensing, is a physical constant given by

$$\Sigma_c = \frac{c^2}{4\pi G} \frac{1}{\beta D_l}, \quad (4.14)$$

which depends on the angular diameter distance to the lens,  $D_l$ , and the lensing efficiency,  $\beta = \max(0, D_{ls}/D_s)$ , for a source at angular diameter distance  $D_s$  from the observer and  $D_{ls}$  from the lens. There is no lensing signal ( $\beta = 0$ ) when the source is in front of the lens, i.e.  $D_{ls} < 0$ .

For a radial, compensated filter obeying the relation

$$\int d\theta \theta U(\theta) = 0, \quad (4.15)$$

Eq. (4.12) can be rewritten in terms of the tangential shear as

$$M_{\text{ap}}(\boldsymbol{\theta}_0) = \int d^2\boldsymbol{\theta} Q(|\boldsymbol{\theta} - \boldsymbol{\theta}_0|) \gamma_T(\boldsymbol{\theta} | \boldsymbol{\theta}_0), \quad (4.16)$$

where the tangential shear is defined as

$$\gamma_T(\theta) = \frac{\bar{\Sigma}(\leq \theta) - \Sigma(\theta)}{\Sigma_c}, \quad (4.17)$$

and the new filter function  $Q(\theta)$  is related to the surface mass density filter  $U(\theta)$  as

$$Q(\theta) = \frac{2}{\theta^2} \int_0^\theta d\theta' \theta' U(\theta') - U(\theta). \quad (4.18)$$

Choosing filters  $U(\theta)$  that are constant within some small inner aperture  $\theta_1$  will result in  $Q(\theta) = 0$  for  $\theta < \theta_1$ . Similarly, compensated filters with  $U(\theta) = 0$  outside  $\theta_m$  give  $Q(\theta) = 0$  for  $\theta > \theta_m$ . Hence, aperture masses can be measured from the tangential shear within some finite region  $\theta_1 < \theta < \theta_m$  for carefully chosen filters  $U$ . The region can be chosen with  $\theta_1$  large enough to avoid the contamination from the densely populated cluster core and, importantly, to ensure measurements within the weak lensing regime. Generally, gravitational lensing does not measure the tangential shear directly, but is instead sensitive to the reduced shear

$$g_T(\theta) = \frac{\gamma_T(\theta)}{1 - \kappa(\theta)}. \quad (4.19)$$

However, if  $\theta_1$  is chosen large enough, then  $\kappa(\theta) \ll 1$  and the weak lensing assumption  $g_T \approx \gamma_T$  holds.

Since galaxy ellipticities are an unbiased estimator of the local shear field in the weak lensing regime, the aperture mass can be estimated directly by summing over the observed galaxy ellipticities (Schneider, 1996). Assuming the mean number density of lensed background galaxies,  $\bar{n}_{\text{gal}}$ , we get

$$M_{\text{ap}}(\boldsymbol{\theta}_0) = \frac{1}{\bar{n}_{\text{gal}}} \sum_i Q(|\boldsymbol{\theta}_i - \boldsymbol{\theta}_0|) \gamma_T(\boldsymbol{\theta}_i). \quad (4.20)$$

The uncertainty in this aperture mass measurement depends only on the shape noise due to the finite number of galaxies sampling the shear field. For an average uncertainty  $\sigma_{\text{gal}}$  in the shear measurement  $\gamma_T$  of an individual galaxy, and a background galaxy number density  $\bar{n}_{\text{gal}}$ , the uncertainty in  $M_{\text{ap}}$  is

$$\sigma_{M_{\text{ap}}(\boldsymbol{\theta}_0)}^2 = \frac{\sigma_{\text{gal}}^2}{\bar{n}_{\text{gal}}} \sum_i Q^2(|\boldsymbol{\theta}_i - \boldsymbol{\theta}_0|). \quad (4.21)$$

The aperture masses that we have used in this paper are directly related to the  $\zeta_c$ -statistic, introduced by Clowe et al. (1998), which can be measured from the tangential shear as

$$\zeta_c(\theta_1) = 2 \int_{\theta_1}^{\theta_2} d \ln \theta \langle \gamma_T \rangle + \frac{2}{1 - \theta_2^2/\theta_m^2} \int_{\theta_2}^{\theta_m} d \ln \theta \langle \gamma_T \rangle. \quad (4.22)$$

We have introduced the tangentially averaged tangential shear,  $\langle \gamma_T \rangle$ , defined as

$$\langle \gamma_T \rangle(\theta) = \frac{1}{2\pi} \oint d\phi \gamma_T(\theta, \phi). \quad (4.23)$$

Eq. (4.22) implies a filter function

$$Q_{\zeta_c}(\theta) = \begin{cases} \frac{1}{\pi\theta^2} & \text{for } \theta_1 < \theta \leq \theta_2 \\ \frac{1}{\pi\theta^2} \frac{\theta_m^2}{\theta_m^2 - \theta_2^2} & \text{for } \theta_2 < \theta \leq \theta_m \\ 0 & \text{elsewhere.} \end{cases} \quad (4.24)$$

We can readily obtain  $\Delta M$  from  $\zeta_c$  as

$$\Delta M(< \theta_1 | \theta_2, \theta_m) = \Sigma_c \zeta_c(< \theta_1) \pi \theta_1^2. \quad (4.25)$$

## 4.B Scalable Gaussian processes for non-Gaussian likelihoods

We start by introducing our notation. For each of the 100 cosmologies,  $\Omega_i$ , simulated in Mira–Titan, we have calculated the aperture mass function  $n(\Delta M, \Omega_i)$  on a log-spaced grid of 50 points with  $\log_{10} \Delta M / M_\odot \in [13.5, 15.5]$  for the redshifts  $z \in \{0.1, 0.24, 0.43, 0.66, 1.0, 1.6, 2.0\}$ . For a set of input locations and observations  $\{(\mathbf{x}_i, N_i) | i = 1, \dots, n\}$ , with  $n = 100 \times 50$  (100 cosmologies with 50 mass bins each), we group the  $1 \times d$ -dimensional input vectors  $\mathbf{x}_i^T$  containing the cosmological parameters and the mass bin, into the rows of the  $n \times d$  matrix  $\mathbf{X}$ , i.e.  $\mathbf{X}_i = \mathbf{x}_i^T$ , and the measured number counts for each redshift  $z_j$  into the  $n$ -dimensional vector  $\mathbf{N}_j$ . We will drop the subscript  $j$  in what follows, since the procedure will be the same for each redshift with only the input measurements differing.

Given the large dynamic range and the peaked nature of the aperture mass function, we do not model the number counts directly. Instead, we predict the number density normalized to the mean value over all cosmologies in the grid

$$f(\mathbf{x}_i) = \log n(\mathbf{x}_i) - \log \langle n(\Delta M_l) \rangle_\Omega, \quad (4.26)$$

with  $\mathbf{x}_i^T = (\Omega_k^T, \Delta M_l)$ , a vector containing the aperture mass for different cosmologies. We stress that a single cosmology,  $\Omega_k$ , has 50 mass bins,  $\Delta M_l$ , and we normalize the aperture mass function with the mean over all cosmologies for each mass bin. This normalization reduces the dynamic range of the latent function  $f(\mathbf{x}_i)$  to values approximately between -1 and 1. We can easily recover the predicted number counts from  $f(\mathbf{x}_i)$  by converting it to  $n(\mathbf{x}_i)$  using Eq. (4.26), and multiplying by the volume element and the bin-spacing in  $\Delta M$ . As long as the mean number density  $\langle n(M_l) \rangle_\Omega > 0$  in Eq. (4.26), the high-mass tail of cosmological models with no observed clusters can be fit consistently with the correct likelihood and without assuming any functional form for the aperture mass function.

To fit this model to the simulated mass functions, we need to assume the likelihood of the simulated data. Since the number counts are discrete observations with exponential cosmology sensitivity in the low-number count, high-mass tail, we cannot assume a Gaussian likelihood that does not accurately describe low

number counts. We cannot assume a Poisson likelihood either, since, as shown in Fig. 4.10, the dispersion of the aperture mass function exceeds the Poisson value. Hence, we assume a negative binomial likelihood for the data  $N_i$  given the model  $f(\mathbf{x}_i)$ . The probability density function of the negative binomial distribution can be written in terms of the mean,  $\mu$ , and the variance,  $\alpha\mu$ , where  $\alpha > 1$  captures the overdispersion compared to the Poisson distribution. In our case, we write the likelihood of the simulated number counts,  $N_i$ , given the model,  $f(\mathbf{x}_i)$ , as

$$p(N_i|f(\mathbf{x}_i)) = \mathcal{NB}(N_i|N(\mathbf{x}_i), \alpha_i), \quad (4.27)$$

where  $N(\mathbf{x}_i)$  is the number of haloes inferred from  $f(\mathbf{x}_i)$ , and  $\alpha_i$  is calculated as the ratio between the bootstrapped variance and the observed number of haloes in the mass bin. Standard Gaussian processes cannot be solved analytically for data with non-Gaussian likelihoods, so we will use the approximate, variational inference Gaussian process method from Hensman et al. (2014) and implemented in GPyTorch<sup>3</sup> (Gardner et al., 2021).

The Gaussian process assumption models the latent function in Eq. (4.26) as (following the notation of Rasmussen & Williams, 2006)

$$f(\mathbf{x}) \sim \mathcal{GP}(\mu, k(\mathbf{x}, \mathbf{x}'|\theta)), \quad (4.28)$$

which is shorthand for

$$\mathbb{E}[f(\mathbf{x})] = \mu, \quad (4.29)$$

$$\text{Var}[f(\mathbf{x}), f(\mathbf{x}')] = k(\mathbf{x}, \mathbf{x}'|\theta), \quad (4.30)$$

and means that the values of  $f$  are fully determined by the mean,  $\mu$ , and the covariance function  $k(\mathbf{x}, \mathbf{x}'|\theta)$  between different inputs  $\mathbf{x}$  and  $\mathbf{x}'$ . We will be using the radial basis function (or squared exponential) kernel for  $k$ :

$$k(\mathbf{x}, \mathbf{x}'|\theta) = \sigma^2 \prod_{i=0}^d \exp\left(-\frac{((\mathbf{x})_i - (\mathbf{x}')_i)^2}{2\ell_i^2}\right), \quad (4.31)$$

where  $i$  runs over the  $d = 9$  dimensions of  $\mathbf{x}$  and each dimension has its own covariance lengthscale  $\ell_i$ , resulting in hyperparameter  $\theta = (\mu, \sigma^2, \ell)$ .

The power of Gaussian process regression stems from the conditioning property of Gaussian distributions. In what follows, we assume  $\mu = 0$  for simplicity. Given the assumed joint Gaussian distribution between function values at  $\mathbf{X}$  and  $\mathbf{X}^*$ ,  $p(\mathbf{f}, \mathbf{f}^*)$ , which we can write as

$$p(\mathbf{f}, \mathbf{f}^*) = p\left(\begin{bmatrix} \mathbf{f} \\ \mathbf{f}^* \end{bmatrix}\right) = \mathcal{N}\left(\begin{bmatrix} \mathbf{0} \\ \mathbf{0} \end{bmatrix}, \begin{bmatrix} K_{\mathbf{XX}} & K_{\mathbf{XX}^*} \\ K_{\mathbf{X}^*\mathbf{X}} & K_{\mathbf{X}^*\mathbf{X}^*} \end{bmatrix}\right), \quad (4.32)$$

the conditional distribution  $p(\mathbf{f}^*|\mathbf{f})$  is a new Gaussian distribution given by

$$p(\mathbf{f}^*|\mathbf{f}, \theta) = \mathcal{N}\left(K_{\mathbf{X}^*\mathbf{X}} K_{\mathbf{XX}}^{-1} \mathbf{f}, K_{\mathbf{X}^*\mathbf{X}^*} - K_{\mathbf{X}^*\mathbf{X}} K_{\mathbf{XX}}^{-1} K_{\mathbf{X}^*\mathbf{X}}\right). \quad (4.33)$$

---

<sup>3</sup><https://github.com/cornellius-gp/gpytorch>

Here we have introduced the  $n \times n$  covariance matrix  $K_{XX}$ , with  $(K_{XX})_{ij} = k(\mathbf{x}_i, \mathbf{x}_j)$  and  $k$  given by Eq. (4.31), containing the covariance between different input points in  $X$ . Importantly, the probability distribution of  $\mathbf{f}^*$  for an arbitrary input location  $X^*$  depends solely on the finite set of *measured* inputs  $X$ . Clearly, the accuracy of the prediction  $f(\mathbf{x}^*)$  depends on the distance to the nearest measured input  $\mathbf{x}$  in  $X$  and the lengthscale hyperparameter  $\ell$ , with the function values  $f^*$  regressing to the mean 0 and prior uncertainty  $k(\mathbf{x}^*, \mathbf{x}^*)$  for  $K_{X^*X} \rightarrow \mathbf{0}^T$ . We can use  $p(\mathbf{f}^*|\mathbf{f}, \theta)$  to predict  $\mathbf{N}(X^*)$ .

The optimal hyperparameters,  $\theta$ , for the simulated data,  $\mathbf{N}$ , are found by maximizing

$$p(\theta|\mathbf{N}) = \frac{p(\theta)p(\mathbf{N}|\theta)}{p(\mathbf{N})}. \quad (4.34)$$

where we introduced the marginal likelihood

$$p(\mathbf{N}|\theta) = \int p(\mathbf{N}|\mathbf{f})p(\mathbf{f}|\theta)d\mathbf{f}, \quad (4.35)$$

which cannot be solved analytically in the case of a negative binomial likelihood.

This standard Gaussian process encounters two major difficulties. First, the  $K_{XX}^{-1}$ -term in Eq. (4.33) becomes computationally expensive for datasets with large  $n$ . Second, non-Gaussian likelihoods require approximations to optimize Eq. (4.34), since no closed-form analytical solution exists. Both of these problems have been solved by the sparse method using inducing variables and the variational free energy as introduced by Titsias (2009) and applied to non-Gaussian likelihoods by Hensman et al. (2014) and formalized by Matthews et al. (2016). We will briefly introduce the necessary ingredients for this method.

The idea behind the method of Titsias (2009) is to introduce both an extra set of  $m \ll n$  inducing (or pseudo) inputs  $Z$  of the Gaussian process such that  $\mathbf{f}(Z) \equiv \mathbf{u}$  and an approximate distribution over these function values,  $q_\psi(\mathbf{u})$ . The inducing point locations  $Z$  and the parameters  $\psi$  of the approximate distribution family will be chosen in such a way that they optimally capture the true posterior probability of the Gaussian process, i.e.  $q_\psi(\mathbf{f}) \simeq p(\mathbf{f}|\mathbf{N})$ . Assuming a Gaussian distribution for  $q(\mathbf{u})$  with

$$q_\psi(\mathbf{u}) = \mathcal{N}(\mathbf{m}, \mathbf{S}), \quad (4.36)$$

we get  $\psi = (\mathbf{m}, \mathbf{S})$  and we calculate the full approximate distribution as

$$q_\psi(\mathbf{f}, \mathbf{u}) = p(\mathbf{f}|\mathbf{u})q_\psi(\mathbf{u}). \quad (4.37)$$

The optimization of  $(Z, \mathbf{m}, \mathbf{S})$  now needs to ensure that

$$\begin{aligned} p(\mathbf{f}|\mathbf{N}) &\simeq \int p(\mathbf{f}|\mathbf{u})q(\mathbf{u})d\mathbf{u} \\ &\Updownarrow p(\mathbf{f}|\mathbf{u}) = \mathcal{N}(K_{XZ}K_{ZZ}^{-1}\mathbf{u}, D_{XX}) \\ &= \mathcal{N}(K_{XZ}K_{ZZ}^{-1}\mathbf{m}, D_{XX} + K_{XZ}K_{ZZ}^{-1}SK_{ZZ}^{-1}K_{ZX}), \end{aligned} \quad (4.38)$$

with  $D_{XX} = K_{XX} - K_{XZ}K_{ZZ}^{-1}K_{ZX}$ , due to the conditioning property of Eq. (4.33) (see Chapter 4.3 of Matthews, 2017 for detailed explanations). Evaluating this expression only requires the inverted  $m \times m$  matrix  $K_{ZZ}^{-1}$ , significantly reducing the computational cost of making model predictions.

To determine the optimal values  $(\mathbf{Z}, \mathbf{m}, \mathbf{S})$ , we minimize the difference between the approximate distribution  $q_\psi(\mathbf{f}, \mathbf{u})$  and the model posterior  $p(\mathbf{f}, \mathbf{u}|\mathbf{N})$  through the Kullback-Leibler (KL) divergence

$$\mathcal{KL}[q(\mathbf{f}, \mathbf{u})||p(\mathbf{f}, \mathbf{u}|\mathbf{N})] = - \int q(\mathbf{f}, \mathbf{u}) \log \left( \frac{p(\mathbf{f}, \mathbf{u}|\mathbf{N})}{q(\mathbf{f}, \mathbf{u})} \right) d\mathbf{f}d\mathbf{u}. \quad (4.39)$$

Defining this equation as  $\mathcal{K}$ , we use Bayes' theorem to rewrite  $p(\mathbf{f}, \mathbf{u}|\mathbf{N}) = p(\mathbf{N}|\mathbf{f})p(\mathbf{f}|\mathbf{u})p(\mathbf{u})/p(\mathbf{N}|\theta)$ , making use of the fact that the observations are only conditionally dependent on their corresponding function values  $\mathbf{f}$ . Also filling in Eq. (4.37), we then find

$$\begin{aligned} \mathcal{K} &= - \int p(\mathbf{f}|\mathbf{u})q(\mathbf{u}) \log \left( \frac{p(\mathbf{N}|\mathbf{f})p(\mathbf{u})}{p(\mathbf{N}|\theta)q(\mathbf{u})} \right) d\mathbf{f}d\mathbf{u} \\ &= - \int q(\mathbf{f}) \log p(\mathbf{N}|\mathbf{f})d\mathbf{f} + \int p(\mathbf{f}|\mathbf{u})q(\mathbf{u}) \log p(\mathbf{N}|\theta)d\mathbf{f}d\mathbf{u} \\ &\quad + \int p(\mathbf{f}|\mathbf{u})q(\mathbf{u}) \log \left( \frac{q(\mathbf{u})}{p(\mathbf{u})} \right) d\mathbf{f}d\mathbf{u} \\ \mathcal{K} &= \log p(\mathbf{N}|\theta) - \mathbb{E}_{q(\mathbf{f})} [\log p(\mathbf{N}|\mathbf{f})] + \mathcal{KL}[q(\mathbf{u})||p(\mathbf{u})]. \end{aligned} \quad (4.40)$$

4

We can rearrange terms in this expression and use the fact that the KL divergence is strictly positive to arrive at the variational evidence lower bound (ELBO), which provides a lower bound on the marginal likelihood—also called the model evidence—as the name suggests

$$\log p(\mathbf{N}|\theta) \geq \mathcal{L}_{\text{ELBO}} = \mathbb{E}_{q(\mathbf{f})} [\log p(\mathbf{N}|\mathbf{f})] - \mathcal{KL}[q(\mathbf{u})||p(\mathbf{u})]. \quad (4.41)$$

Equality for this equation holds exactly when Eq. (4.39) equals zero, which is the case when  $q(\mathbf{f}, \mathbf{u}) = p(\mathbf{f}, \mathbf{u}|\mathbf{N})$ . Assuming no covariance between  $f_i$  and  $N_{j \neq i}$ , the likelihood factors and we have

$$\mathcal{L}_{\text{ELBO}} = \sum_{i=1}^n \mathbb{E}_{q(f_i)} [\log p(N_i|f_i)] - \mathcal{KL}[q(\mathbf{u})||p(\mathbf{u})], \quad (4.42)$$

where the first term consists of a sum of one dimensional integrals which can be computed easily using Gauss-Hermite quadrature, and the second term is the KL divergence between two multivariate Gaussian distributions, since  $p(\mathbf{u}) = \mathcal{N}(\mathbf{0}, \mathbf{K}_{ZZ})$  due to the Gaussian process assumption. Optimizing the ELBO is equivalent to maximizing the marginal log-likelihood in Eq. (4.35).

We use the `ApproximateGP`<sup>4</sup> implementation of GPyTorch to model and optimize  $f(\mathbf{x}_i)$  with a custom implementation of the negative binomial likelihood between  $N(\mathbf{x}_i)$  and the measurements number counts from the simulations,  $N_i$ .

<sup>4</sup>[https://docs.gpytorch.ai/en/latest/examples/04\\_Variational\\_and\\_Approximate\\_GPs/Non\\_Gaussian\\_Likelihoods.html](https://docs.gpytorch.ai/en/latest/examples/04_Variational_and_Approximate_GPs/Non_Gaussian_Likelihoods.html)

## 4.C Emulator performance

The approximate Gaussian process does not sample the simulation inputs, but instead optimizes the inducing point locations to accurately reproduce the posterior of the full Gaussian process, i.e. Eq. (4.39). Hence, we will not trivially reproduce the simulation aperture mass function. In our set-up, we first normalize the input parameters,  $\mathbf{X}$ , so that all parameters lie between 0 and 1. We use 500 inducing points in the `ApproximateGP` variational distribution and minimize the marginal likelihood, approximated by the `gpytorch.mlls.VariationalELBO`, with the Adam optimizer with a learning rate of 0.01 and mini-batches of 512 observations each. These settings resulted in the fastest loss function minimization in a coarse, manual search for the optimal parameter settings. We resample the initial hyperparameters 5 times from their uniform priors to avoid local minima in the optimization. The emulator parameters are specified by the inducing point locations,  $\mathbf{u}$ , from Eq. (4.36) in Appendix 4.B, the Gaussian process mean,  $\mu$ , from Eq. (4.29), and the kernel lengthscales and normalization,  $\ell$  and  $\sigma$ , respectively, from Eq. (4.31). We choose uniform priors  $\mathbf{u} \sim \mathcal{U}(0, 1)$ ,  $\mu \sim \mathcal{U}(-1, 1)$ ,  $\ell \sim \mathcal{U}(0.05, 2.0)$ , and  $\sigma^2 \sim \mathcal{U}(0.05, 2.0)$ .

In the top row of Fig. 4.15, we show the resulting absolute deviation between the emulated latent function, Eq. (4.26), and the normalized number density from the simulation for different apertures and all cosmologies. The first three columns correspond to the different aperture sizes at  $z = 0.43$ , and the final column shows the median and 16th to 84th percentile scatter for the emulator at different redshifts. For low aperture masses, the emulator error rarely exceeds the 5 per cent difference level, and the bulk of the simulations have residuals within  $\pm 2$  per cent for the high abundance aperture mass regime. The median deviation is biased slightly low for  $R_1 = 1.0 \text{ cMpc}$ , but it is within  $\pm 2$  per cent for all aperture sizes and all but the most massive haloes. The bulk of the simulations lack haloes at the highest aperture masses resulting in the noticeable downturn. While the fractional deviation becomes large, it is still within the variance of the simulations, which is shown as the shaded region.

To quantify the quality of the fit in the high-mass tail, we show the equivalent Gaussian significance of the deviation between the simulated data and the emulator. We compute the significance by calculating the difference between the log-likelihood of the measured number counts in the simulation given the predicted aperture mass function of the emulator,  $\ln \mathcal{L}(N_{\text{true}}|N_{\text{pred}})$ , and the log-likelihood of the emulated number counts,  $\ln \mathcal{L}(N_{\text{pred}}|N_{\text{pred}})$ , and converting this probability ratio into the equivalent Gaussian confidence interval  $n\sigma$  around the mean expectation,  $\mu$ , given by  $\ln P(\mu + n\sigma) - \ln P(\mu)$ . We show the significance of the deviation between the emulator and the simulation data in the bottom row of Fig. 4.15. Individual simulations behave erratically for low aperture masses, rapidly oscillating between large and small significance, but rarely exceeding  $3\sigma$ . The median significance of all cosmologies, on the other hand, is consistently  $\approx 1\sigma$ . For the high-aperture mass tail, with large fractional deviations between the emulator and the simulations, the significance of the deviation  $\lesssim 1\sigma$ , indicating that

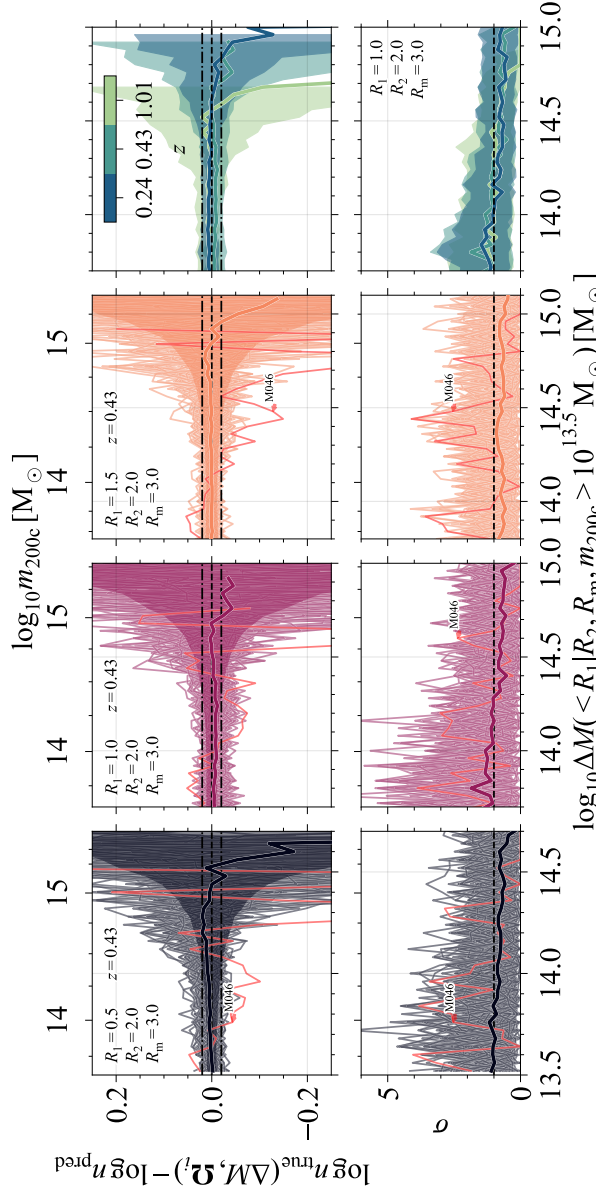


Figure 4.15: *Top row:* The residuals between the best-fit emulator and the individual simulations in the hypercube for different apertures at fixed redshift  $z = 0.43$  (*first three columns*) and at different redshifts for a fixed aperture  $(R_1, R_2, R_m) = (1, 2, 3)$  cmpc (*rightmost column*). All halo samples were selected with  $m_{200c} > 10^{13.5} M_\odot$ . For the aperture variations, we show the individual simulations and for the redshift variations the 16th to 84th percentile scatter to avoid clutter. The thick, coloured line indicates the median emulator residual and the shaded regions in the aperture plots indicate the median of the bootstrapped simulation uncertainties. The black, dash-dotted lines indicate the  $\pm 2$  per cent deviation. The median emulator residual is within the simulation uncertainty, and unbiased for low aperture masses and  $R_1 = 0.5, 1.5$  cmpc, while biased low at the  $\approx 1$  per cent level for  $R_1 = 1.0$  cmpc. For abundant, low-aperture mass haloes the emulator reaches an accuracy of  $\approx 2$  per cent for the bulk of the simulations, rarely exceeding the 5 per cent level. The most significant outlier, M046, which was run with a smaller box size, is indicated with a red line in the different panels. *Bottom row:* The Gaussian-equivalent significance of the likelihood ratio between the simulated data and the emulator. The median significance is mostly  $\approx 1\sigma$ . The significance for the individual simulations can vary wildly, but, as the top row shows, the fractional uncertainty remains reasonable.

the emulator captures the trends in the data to within the shot-noise.

Finally, we also perform a leave-one-out test on all simulations that are not at the edge of the parameter space for any of the cosmological parameters. In Fig. 4.16, we show how accurately the emulator predicts the aperture mass function for all left-out simulations. We colour the lines for simulations with cosmological parameters that are within the first or the last decile of the hypercube with different shades of blue and red, respectively, with darker shades indicating more significant outliers. The emulator can predict the outcome of most simulations to within  $\approx 5$  per cent up to the tail of the mass function. The most significant deviations are found for simulations that are close to the edge of the cosmological parameter space in one or more dimensions. The accuracy achieved by the emulator in the leave-one-out test indicates that the emulator generalizes well beyond the trained simulation inputs.

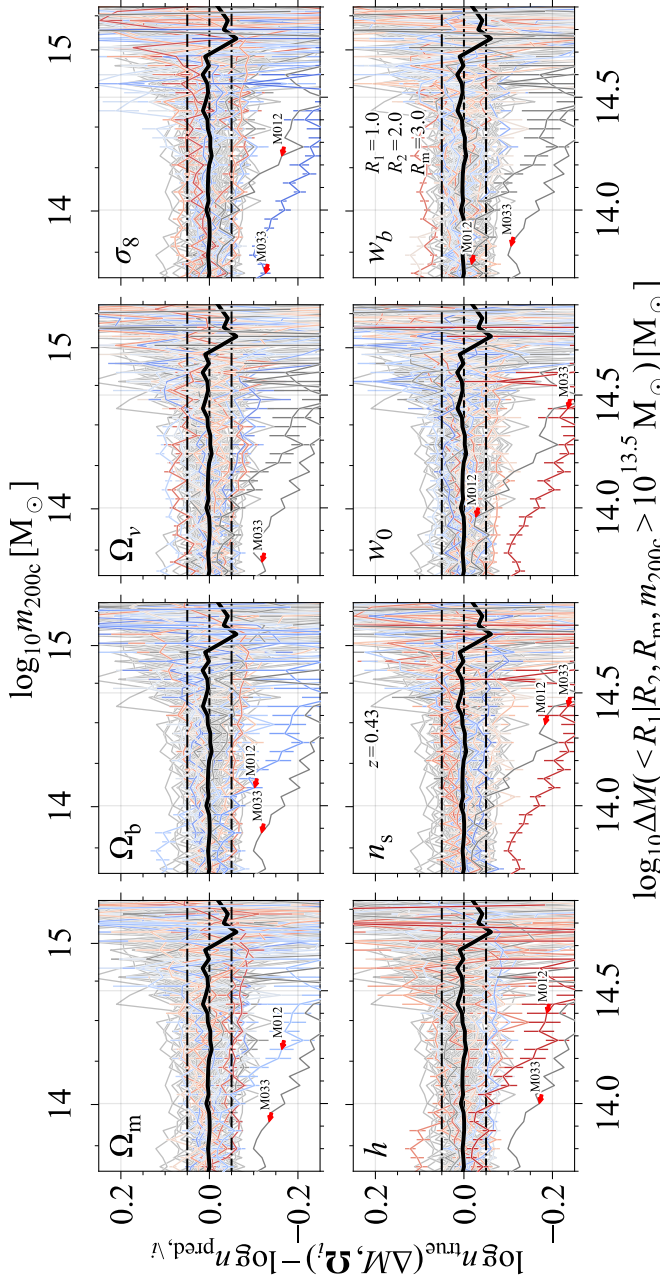


Figure 4.16: The residuals between the leave-one-out emulator and its held out simulation for all simulations that are not at the edge of the parameter space. The cosmological parameters are indicated in the top-left corner of each panel. All emulators have apertures  $(R_1, R_2, R_m) = (1, 2, 3)$  cMpc and have been calibrated at  $z = 0.43$ . All halo samples were selected with  $m_{200c} > 10^{13.5} M_\odot$ . Coloured lines indicate the simulations that are within the first (blue shades) or last (red shades) decile for the plotted cosmological parameter, with the saturation indicating the ordering. The black line indicates the median result for all simulations and the shaded region the 16th to 84th percentile scatter. The black, dash-dotted lines indicate the  $\pm 5$  per cent region. Most emulators are able to reproduce the held out simulation prediction within  $\approx 5$  per cent. The most significant outliers, M012 and M033, are indicated with red arrows and are simulations that are close to the edge of the parameter space for several cosmological parameters.

## Bibliography

- Aguena M., Lima M., 2018, Phys. Rev. D, 98, 123529
- Allen S. W., Evrard A. E., Mantz A. B., 2011, Annu. Rev. Astron. Astrophys., 49, 409
- Andreon S., Congdon P., 2014, A&A, 568, A23
- Angulo R. E., Springel V., White S. D. M., Jenkins A., Baugh C. M., Frenk C. S., 2012, Mon. Not. R. Astron. Soc., 426, 2046
- Applegate D. E., et al., 2014, Mon. Not. R. Astron. Soc., 439, 48
- Bahcall N. A., Kulier A., 2014, Monthly Notices of the Royal Astronomical Society, 439, 2505
- Bahé Y. M., McCarthy I. G., King L. J., 2012, Mon. Not. R. Astron. Soc., 421, 1073
- Bartelmann M., Schneider P., 2001, Physics Reports, 340, 291
- Becker M. R., Kravtsov A. V., 2011, Astrophys. J., 740
- Bhattacharya S., Heitmann K., White M., Lukic Z., Wagner C., Habib S., 2011, Astrophys. J., 732, 122
- Bleem L. E., et al., 2020, Astrophys. J. Suppl. Ser., 247, 25
- Bocquet S., Heitmann K., Habib S., Lawrence E., Uram T., Frontiere N., Pope A., Finkel H., 2020, Astrophys. J., 901, 5
- Bond J. R., Cole S., Efstathiou G., Kaiser N., 1991, Astrophys. J., 379, 440
- Budzynski J. M., Koposov S. E., McCarthy I. G., Belokurov V., 2014, Mon. Not. R. Astron. Soc., 437, 1362
- Chon G., Böhringer H., 2017, Astron. Astrophys., 606, L4
- Clowe D., Luppino G. A., Kaiser N., Henry J. P., Gioia I. M., 1998, Astrophys. J., 497, L61
- Crocce M., Fosalba P., Castander F. J., Gaztañaga E., 2010, Monthly Notices of the Royal Astronomical Society, 403, 1353
- Cromer D., Battaglia N., Miyatake H., Simet M., 2021, arXiv:2104.06925 [astro-ph]
- DES Collaboration et al., 2020, Phys. Rev. D, 102, 023509
- Debackere S. N. B., Schaye J., Hoekstra H., 2021, Monthly Notices of the Royal Astronomical Society, 505, 593
- Debackere S. N. B., Hoekstra H., Schaye J., 2022, Galaxy Cluster Aperture Masses Are More Robust to Baryonic Effects than 3D Halo Masses ([arXiv:2205.08424](https://arxiv.org/abs/2205.08424)), doi:10.48550/arXiv.2205.08424
- Despali G., Giocoli C., Angulo R. E., Tormen G., Sheth R. K., Baso G., Moscardini L., 2016, Mon. Not. R. Astron. Soc., 456, 2486
- Diemer B., 2020, ApJ, 903, 87
- Dietrich J. P., Hartlap J., 2010, Mon. Not. R. Astron. Soc., 402, 1049
- Dietrich J. P., et al., 2019, Mon. Not. R. Astron. Soc., 483, 2871
- Erickson B. M. S., Cunha C. E., Evrard A. E., 2011, Phys. Rev. D, 84, 103506
- Gardner J. R., Pleiss G., Bindel D., Weinberger K. Q., Wilson A. G., 2021, arXiv:1809.11165 [cs, stat]
- Grandis S., Bocquet S., Mohr J. J., Klein M., Dolag K., 2021, Monthly Notices of the Royal Astronomical Society, 507, 5671
- Habib S., et al., 2016, New Astronomy, 42, 49
- Haiman Z., Mohr J. J., Holder G. P., 2001, Astrophys. J., 553, 545
- Hallman E. J., O'Shea B. W., Burns J. O., Norman M. L., Harkness R., Wagner R., 2007, ApJ, 671, 27
- Hamana T., Sakurai J., Koike M., Miller L., 2015, Publications of the Astronomical

- Society of Japan, 67, 34
- Heitmann K., et al., 2016, *Astrophys. J.*, 820, 108
- Heitmann K., et al., 2019, *ApJS*, 244, 17
- Hennawi J. F., Spergel D. N., 2005, *Astrophys. J.*, 624, 59
- Hensman J., Matthews A., Ghahramani Z., 2014, arXiv:1411.2005 [stat]
- Henson M. A., Barnes D. J., Kay S. T., McCarthy I. G., Schaye J., 2017, *Mon. Not. R. Astron. Soc.*, 465, 3361
- Hoekstra H., 2001, *Astron. Astrophys.*, 370, 743
- Hoekstra H., 2003, *Mon. Not. R. Astron. Soc.*, 339, 1155
- Hoekstra H., Mahdavi A., Babul A., Bildfell C., 2012, *Monthly Notices of the Royal Astronomical Society*, 427, 1298
- Hoekstra H., Bartelmann M., Dahle H., Israel H., Limousin M., Meneghetti M., 2013, *Space Sci. Rev.*, 177, 75
- Hoekstra H., Herbonnet R., Muzzin A., Babul A., Mahdavi A., Viola M., Cacciato M., 2015, *Monthly Notices of the Royal Astronomical Society*, 449, 685
- Köhlinger F., Hoekstra H., Eriksen M., 2015, *Mon. Not. R. Astron. Soc.*, 453, 3107
- Kratochvil J. M., Haiman Z., May M., 2010, *Physical Review D*, 81, 043519
- Lawrence E., et al., 2017, *Astrophys. J.*, 847, 50
- Le Brun A. M. C., McCarthy I. G., Melin J. B., 2015, *Mon. Not. R. Astron. Soc.*, 451, 3868
- Mandelbaum R., Seljak U., Baldauf T., Smith R. E., 2010, *Monthly Notices of the Royal Astronomical Society*, 405, 2078
- Mantz A. B., 2019, *Mon. Not. R. Astron. Soc.*, 485, 4863
- Mantz A., Allen S. W., Ebeling H., Rapetti D., Drlica-Wagner A., 2010a, *Monthly Notices of the Royal Astronomical Society*, 406, 1773
- Mantz A., Allen S. W., Rapetti D., Ebeling H., 2010b, *Mon. Not. R. Astron. Soc.*, 406, 1759
- Marian L., Smith R. E., Bernstein G. M., 2009, *Astrophys. J.*, 698, 33
- Marian L., Smith R. E., Bernstein G. M., 2010, *Astrophys. J.*, 709, 286
- Martinet N., et al., 2018, *Monthly Notices of the Royal Astronomical Society*, 474, 712
- Matthews A. G. d. G., 2017, Thesis, University of Cambridge, doi:10.17863/CAM.25348
- Matthews A. G. d. G., Hensman J., Turner R., Ghahramani Z., 2016, in *Proceedings of the 19th International Conference on Artificial Intelligence and Statistics*. PMLR, pp 231–239
- McClintock T., et al., 2019, *Astrophys. J.*, 872, 53
- Nishimichi T., et al., 2019, *Astrophys. J.*, 884, 29
- Oguri M., Hamana T., 2011, *Mon. Not. R. Astron. Soc.*, 414, 1851
- Planck Collaboration et al., 2020, *Astron. Astrophys.*, 641, A6
- Pratt G. W., Arnaud M., Biviano A., Eckert D., Ettori S., Nagai D., Okabe N., Reiprich T. H., 2019, *Space Science Reviews*, 215, 25
- Press W. H., Schechter P., 1974, *Astrophys. J.*, 187, 425
- Rasmussen C. E., Williams C. K. I., 2006, *Gaussian Processes for Machine Learning*. Adaptive Computation and Machine Learning, MIT Press, Cambridge, Mass
- Reblinsky K., Bartelmann M., 1999, *Astron. Astrophys.*, 345, 1
- Saro A., et al., 2015, *Monthly Notices of the Royal Astronomical Society*, 454, 2305
- Sartoris B., et al., 2016, *Mon. Not. R. Astron. Soc.*, 459, 1764
- Schneider P., 1996, *Mon. Not. R. Astron. Soc.*, 283, 837
- Schneider P., Van Waerbeke L., Jain B., Kruse G., 1998, *Mon. Not. R. Astron. Soc.*, 296, 873

- Shan H., et al., 2018, Monthly Notices of the Royal Astronomical Society, 474, 1116
- Shirasaki M., Nagai D., Lau E. T., 2016, Monthly Notices of the Royal Astronomical Society, 460, 3913
- Smith R. E., Marian L., 2011, Monthly Notices of the Royal Astronomical Society, 418, 729
- Tinker J., Kravtsov A. V., Klypin A., Abazajian K., Warren M., Yepes G., Gottlöber S., Holz D. E., 2008, *Astrophys. J.*, 688, 709
- Titsias M., 2009, in Proceedings of the Twelfth International Conference on Artificial Intelligence and Statistics. PMLR, pp 567–574
- Upadhye A., Biswas R., Pope A., Heitmann K., Habib S., Finkel H., Frontiere N., 2014, *Phys. Rev. D*, 89, 103515
- Velliscig M., van Daalen M. P., Schaye J., McCarthy I. G., Cacciato M., Le Brun A. M., Vecchia C. D., 2014, *Mon. Not. R. Astron. Soc.*, 442, 2641
- Voit G. M., Evrard A. E., Bryan G. L., 2001, *ApJ*, 548, L123
- Von der Linden A., et al., 2014, *Mon. Not. R. Astron. Soc.*, 439, 2
- Wang S., Haiman Z., May M., 2009, *The Astrophysical Journal*, 691, 547
- Wang C., et al., 2018, Monthly Notices of the Royal Astronomical Society, 475, 4020
- Yang X., Kratochvil J. M., Wang S., Lim E. A., Haiman Z., May M., 2011, *Phys. Rev. D*, 84, 043529
- Zhang Y., Annis J., 2022, *Monthly Notices of the Royal Astronomical Society: Letters*, 511, L30
- Zu Y., Mandelbaum R., 2015, *Mon. Not. R. Astron. Soc.*, 454, 1161
- van Haarlem M. P., Frenk C. S., White S. D. M., 1997, *Monthly Notices of the Royal Astronomical Society*, 287, 817

